

THEORETICAL STUDY OF BOSE-EINSTEIN CONDENSATE IN AN OPTICAL RATCHET POTENTIAL

A Thesis Presented to the Department of Theoretical and Applied Physics

African University of Science and Technology, Abuja

In partial fulfilment of the requirements for the award

MASTER OF SCIENCE DEGREE

By

Joshua Christopher

Supervised by
Prof. Dr. Kenfack Anatole



African University of Science and Technology
P.M.B 681, Garki, Abuja F.C.T, Nigeria.

June, 2019

Abstract

Transport phenomena play a central role in many areas of physics, chemistry, and biology. A particularly intriguing example is the ratchet effect, in which particles develop a directed current along a periodic structure even without an applied bias force. This concept, first explored by Smoluchowski and later by Feynman, was initially inspired by the operation of molecular motors in biological systems. Today, ratchet models find wide applications, especially in cases where particle mass significantly influences the dynamics, introducing complexities such as chaos and current reversals. In this work, we aim to construct a model of directed transport for particles diffusing in a ratchet potential. Our focus is on a Bose–Einstein Condensate (BEC) subjected to periodic temporal modulation. The dynamics of such a system are governed by the Gross–Pitaevskii Equation (GPE), which we solve numerically using the Split Operator Method. While many theoretical and experimental studies have examined similar setups with symmetric potentials, our approach specifically considers an asymmetric ratchet potential. Within this framework, we will compute key observables—including the current, condensate energy, and the number of non-condensate particles—with particular attention to the role of quantum resonance.

Dedication

This thesis is dedicated to my mother, whose unconditional love, prayers, and unwavering support have been my greatest source of strength. I am also deeply grateful to PAMI for awarding me the scholarship that enabled my studies at the African University of Science and Technology. Finally, I extend my heartfelt thanks to my friends and family for their encouragement and support throughout this journey.

Declaration

This is to certify that the thesis entitled “Bose–Einstein Condensate in a Ratchet Optical Potential”, submitted to the School of Postgraduate Studies at the African University of Science and Technology (AUST), Abuja, Nigeria, in partial fulfillment of the requirements for the award of the Master’s degree, is an original work carried out by Joshua Christopher in the Department of Physics.

Contents

1	Introduction	5
1.1	Bose Einstein Condensate and Subatomic particles	5
1.2	Bose Einstein Condensation	6
2	Theoretical Background	7
2.1	Introduction	7
2.2	The Gross-Pitaevskii Equation	7
2.3	The Gross-Pitaevskii Equation	8
2.4	Ground State of Trapped Boson	11
2.5	The Variational Approximation	12
2.6	Thomas-Fermi Approximation	14
2.7	Dimensional Reduction of the Gross-Pitaevskii Equation	15
2.7.1	Quasi-1D Reduction	15
2.8	Hydrodynamic Formulation of the Gross–Pitaevskii Equation	16
2.9	GPE in 1D with Harmonic Oscillator Potential	17
2.10	Vortices in Optics and Bose–Einstein Condensates	17
2.11	Bright Solitons in Nonlinear Dispersive Media	18
2.12	Dark Solitons in Bose–Einstein Condensates	19
2.13	Dynamical Instabilities and Excitations in Vortices and Dark Solitons .	20
3	Numerical Methods	21
3.1	Numerical Method	21
3.2	Lie Splitting Method (LSM)	22
3.3	Strang Splitting Spectral Method (SSM)	22
3.4	Error Estimates	23
3.5	Error Analysis for Constant Potential	24
4	Results and Discussion	26
4.1	Introduction	26
4.2	Results Presentation	26
4.2.1	GPE Equation with external trapping potential $V = 0$	27
4.2.2	Dark Soliton Solution Derivation	32
4.3	Numerical Study of the Bose Einstein Condensate in an Optical Ratchet Potential	36
4.4	Split Operator Method	36
4.5	Implementation Details	37
4.6	Time-Dependent Penrose–Onsager Analysis	38
4.6.1	Physical Observables	38

4.6.2	Numerical Results and Interpretations	39
4.6.3	Density Evolution	39
4.6.4	Condensate vs Non-Condensate Fraction	41
4.6.5	Energy Contributions and their effect on condensate and non condensate fractions	43
4.6.6	Current and average motion of the condensate	48
4.7	Conclusion	50
4.8	Future Outlook	51

Chapter 1

Introduction

1.1 Bose Einstein Condensate and Subatomic particles

There are three basic states of matter familiar to humans: solid, liquid and gas. However, scientists recognize additional states beyond these three. The fourth state of matter is plasma, which consists of a cloud of positively charged ions and free electrons, where the electrons have become detached from their respective atoms or molecules. Plasma occurs in high-energy processes such as flames, lightning, the cores of stars, and the Sun's corona [1]. The fifth state of matter known as a Bose–Einstein condensate (BEC), was first proposed theoretically by Satyendra Nath Bose and Albert Einstein in the 1920s [2, 3]. A BEC forms when a group of bosons is cooled to temperatures near absolute zero, causing them to occupy the same quantum state and behave as a single quantum entity. This phenomenon was experimentally observed for the first time in 1995 by Eric Cornell and Carl Wieman using rubidium-87 atoms [4].

Before discussing the physics of Bose–Einstein condensates in detail, it is useful to review subatomic particles. A subatomic particle is any particle smaller than an atom. These can be either elementary particles or composite particles. Particle physics focuses on the study of such particles, their interactions, and forms of matter composed of them that do not necessarily aggregate into atoms [5]. Elementary particles are particles with no known substructure, meaning they are not composed of smaller constituents. They form the fundamental building blocks of the universe from which atoms are made. Examples include quarks, leptons (such as electrons), and gauge bosons (such as photons) [6]. Composite particles, by contrast, are made of two or more elementary particles bound together. For example, protons are baryons made up of two up quarks and one down quark, bound by the strong force via gluons [7]. Mesons are another type of composite particle, consisting of a quark–antiquark pair. All known particles can be classified as fermions or bosons. Fermions are particles that follow Fermi–Dirac statistics and obey the Pauli exclusion principle, which states that no two identical fermions can occupy the same quantum state simultaneously [8]. This means that if one fermion is in the lowest energy state, another identical fermion must be in a higher energy state. Fermions have half-integer spin values (e.g., $\frac{1}{2}, \frac{3}{2}, \frac{5}{2}, \dots$) and include particles such as electrons, protons, and neutrons. Bosons, in contrast, follow Bose-Einstein statistics and do not obey the Pauli exclusion principle. They can occupy the same quantum state, enabling phenomena

like laser light and superfluidity. Bosons have integer spin values (e.g., 0, 1, 2, ...) and include force-carrying particles such as photons, gluons, and the Higgs boson [2, 9].

1.2 Bose Einstein Condensation

The Bose-Einstein condensate constitutes a quantum mechanical phase that emerges when a dilute gas of bosons is cooled to temperatures approaching absolute zero (< 100 nK). Under these conditions, the de Broglie wavelengths of particles overlap significantly, causing them to occupy the same quantum ground state [4]. The particle density in BECs is remarkably low ($\sim 10^{13}$ - 10^{15} atoms/cm 3) compared to conventional matter, yet quantum effects dominate due to the extreme cooling. This state exhibits macroscopic quantum phenomena such as superfluidity and coherent matter-wave propagation [10]. The transition to BEC occurs when the thermal de Broglie wavelength exceeds the average interparticle spacing, satisfying the condition for quantum degeneracy. The density contrast between these states is particularly striking when comparing ordinary matter to extreme conditions. While nuclear matter reaches densities of $\sim 10^{38}$ nucleons/cm 3 [10], and conventional solids maintain $\sim 10^{23}$ atoms/cm 3 , the BEC exists at densities several orders of magnitude lower than ambient gases. This low-density regime enables the observation of quantum mechanical effects on macroscopic scales, provided the system is cooled to microkelvin temperatures. In contrast, quantum behavior in solids typically requires only moderately low temperatures, as seen in superconductivity phenomena occurring at temperatures up to 138 K [11].

Although the concept of BEC was predicted theoretically in 1924 by the combined efforts of Satyendra Nath Bose and Albert Einstein, its experimental realization came more than seventy years later. In 1995, the JILA group, led by Eric Cornell and Carl Wieman, reported the creation of a BEC in a dilute gas of rubidium-87 atoms, publishing their results on July 14, 1995 [4]. A few months later, on November 24, 1995, the MIT group, led by Wolfgang Ketterle, reported the condensation of sodium atoms [12]. Since these pioneering experiments, the field of BEC research has grown rapidly, with important developments in both theory and experiment. BEC studies now influence multiple areas of physics, including atomic physics, nuclear physics, and optical physics. Currently, there are more than a hundred research groups worldwide investigating BEC systems. Following its realization in rubidium and sodium, scientists have experimentally produced BECs in various other systems, including hydrogen, metastable helium, lithium, potassium, ytterbium, and even diatomic molecules such as Li₂ [13].

Chapter 2

Theoretical Background

2.1 Introduction

Bose-Einstein condensation (BEC) was first predicted theoretically by S. N. Bose and A. Einstein in the 1920s [2, 3]. The phenomenon was experimentally realized in 1995 through landmark experiments on dilute atomic vapors of rubidium and sodium. In these experiments, atoms were confined in magnetic traps and cooled to temperatures on the order of a few hundred nanokelvins [4, 12]. Evidence for condensation was obtained using time-of-flight measurements: the trapping potential was turned off, allowing the atomic cloud to expand, and optical imaging was used to record the velocity distribution. Below a critical temperature, a sharp peak appeared in the velocity distribution, indicating the formation of a Bose-Einstein condensate, in which a macroscopic fraction of atoms occupy the lowest quantum state [14].

2.2 The Gross-Pitaevskii Equation

A natural starting point for studying the behavior of Bose-Einstein condensates is the theory of weakly interacting bosons. For inhomogeneous systems, this is described by the Gross-Pitaevskii (GP) theory, which provides a mean-field approach for the condensate order parameter. The GP theory yields a closed-form, relatively simple equation that captures the essential properties and dynamics of the condensate. The Gross-Pitaevskii equation can be expressed as:

$$i\hbar \frac{\partial \psi}{\partial t} = \left(-\frac{\hbar^2}{2m} \nabla^2 + V_{\text{ext}}(\mathbf{r}) + g|\psi|^2 \right) \psi \quad (2.1)$$

where ψ is the wave function of the condensate, m is the mass of the particles, V_{ext} is the external potential, and g is the interaction strength.

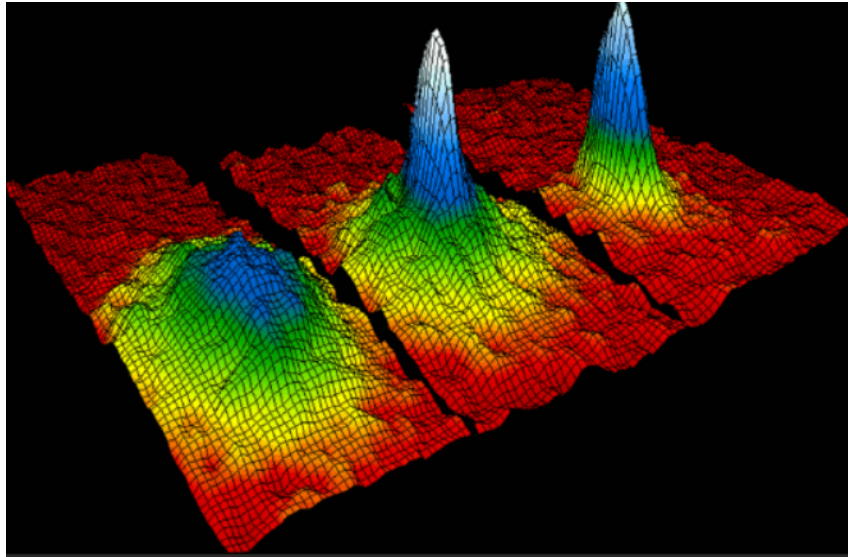


Figure 2.1: Images of the velocity distribution of rubidium atoms in the experiment by Anderson et al. [4], taken by means of the expansion method. The left frame corresponds to a gas at a temperature just above condensation; the center frame, just after the appearance of the condensate; the right frame, after further evaporation leaves a sample of nearly pure condensate. The field of view is $200\mu m \times 270\mu m$, and corresponds to the distance the atoms have moved in about $\frac{1}{20}$ s. The color corresponds to the number of atoms at each velocity, with red being the fewest and white being the most.

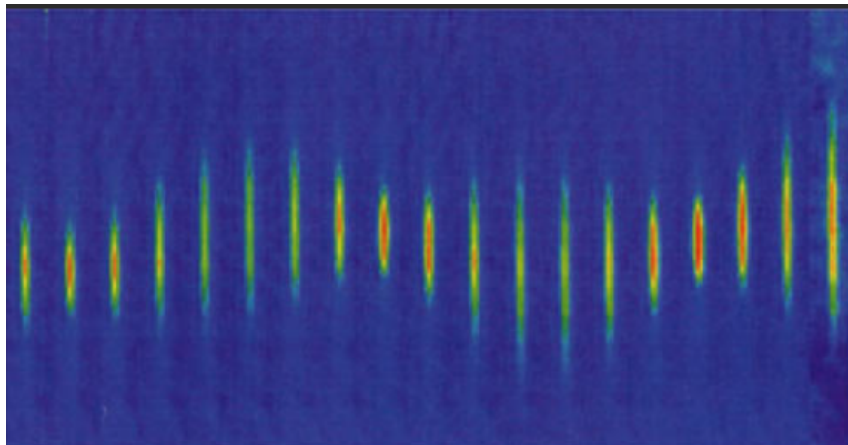


Figure 2.2: Collective excitations of a Bose-Einstein condensate. Shown are in-situ repeated phase-contrast images taken of a "pure" condensate. The excitations were produced by modulating the magnetic fields which confine the condensate, and then letting the condensate evolve freely. Both the center-of-mass and the shape oscillations are visible, and the ratio of their oscillation frequencies can be accurately measured. The field of view in the vertical direction is about $620\mu m$, corresponding to a condensate width of the order of $200 - 300\mu m$. The time step is 5 ms per frame [88].

2.3 The Gross-Pitaevskii Equation

The Gross-Pitaevskii equation describes the ground state of a quantum system of identical bosons within the mean-field approximation, employing the Hartree-Fock method and

a contact interaction potential model [15, 16]. Here, we derive the Gross-Pitaevskii equation using the variational approach, a powerful technique for approximating solutions to systems with infinitely many degrees of freedom by reducing them to finite-dimensional problems [24]. The variational approximation can be summarized in the following steps:

1. Determine the Lagrangian or Hamiltonian of the governing equation.
2. Choose a suitable trial wave function that contains a finite number of parameters, called variational parameters. These parameters may depend on spatial and temporal variables and can include quantities such as the amplitude, phase, width, or orientation of the wave function.
3. Substitute the trial wave function into the Lagrangian and perform the resulting sums if the system is discrete or integrals if the system is continuous.
4. Derive the Euler-Lagrange equations, which yield ordinary differential equations for the variational parameters. These equations can then be solved either numerically or analytically to investigate the system's dynamics.

For dilute ultracold gases at low energies, the interatomic interactions are fully characterized by the s-wave scattering length a [14]. The interaction potential can be replaced by an effective contact potential:

$$H = \sum_{n=1}^N \left(\frac{p_n^2}{2m} + V(\mathbf{r}_n) \right) + \frac{1}{2} \sum_{n=1}^N \sum_{i \neq n}^N L(\mathbf{r}_n - \mathbf{r}_i), \quad (2.2)$$

where the first term represents the kinetic energy (with p_n as the momentum and m as the mass), V is the external trapping potential, and L is the two-body interaction potential. The Hartree approximation is used to seek the ground state of the system. The central idea of this approximation is that each boson experiences the same mean-field potential due to all other bosons, allowing the many-body wave function to be approximated as a product of identical single-particle wave functions. For the N -body system, we take a trial wave function of the form:

$$\theta_N(\mathbf{r}_1, \mathbf{r}_2, \dots, \mathbf{r}_N, t) = \prod_{n=1}^N \phi(\mathbf{r}_n, t), \quad (2.3)$$

where ϕ denotes the single-particle wave function. In a dilute ultra-cold gas at low energies, atoms are described by the *s*-wave scattering length, denoted by a [13], which can be positive or negative. A positive a corresponds to repulsive interactions between the atoms in the BEC, whereas a negative a indicates attractive interactions. For example, BECs formed from sodium atoms exhibit repulsive interactions, while those formed from lithium atoms exhibit attractive interactions. Once the atomic scattering length is known, either theoretically or experimentally, one can replace the actual inter-atomic potential with a delta-function pseudo-potential that reproduces the same scattering length. This allows the interaction potential to be expressed effectively as:

$$L(\mathbf{r}_j - \mathbf{r}_i) = g\delta(\mathbf{r}_j - \mathbf{r}_i) \quad (2.4)$$

where $g = \frac{4\pi\hbar^2 a}{m}$, a denotes the atomic scattering length and m is the mass of the particle. Since $p_n = -i\hbar\nabla_n$, the Hamiltonian of the system can be rewritten as:

$$H = \sum_{n=1}^N \left(-\frac{\hbar^2}{2m} \nabla_n^2 + V(\mathbf{r}_n) \right) + \frac{g}{2} \sum_{n=1}^N \sum_{i \neq n}^N \delta(\mathbf{r}_n - \mathbf{r}_i) \quad (2.5)$$

The total Lagrangian of the system is given as:

$$L = \int_{-\infty}^{\infty} \prod_{k=1}^N d\mathbf{r}_k \left[\frac{i\hbar}{2} \left(\theta_N^* \frac{\partial \theta_N}{\partial t} - \frac{\partial \theta_N^*}{\partial t} \theta_N \right) - \sum_{n=1}^N \left(\frac{\hbar^2}{2m} |\nabla_n \theta_N|^2 + V(\mathbf{r}_n) |\theta_N|^2 + \frac{g}{2} \sum_{i \neq n}^N \delta(\mathbf{r}_n - \mathbf{r}_i) |\theta|^2 \right) \right] \quad (2.6)$$

Substituting equation (2.2) into (2.5) using the fact that $\theta(\mathbf{r}_n, t) = \phi(\mathbf{r}_n, t)$, the first term in the equation can be written as:

$$\int_{-\infty}^{\infty} \prod_{k=1}^N d\mathbf{r}_k \frac{i\hbar}{2} \theta_N^* \frac{\partial \theta_N}{\partial t} = \frac{i\hbar}{2} \sum_{l=1}^N \left(\int_{-\infty}^{\infty} d\mathbf{r}_l \phi_l^* \cdot \frac{\partial \phi_l}{\partial t} \right) \left(\prod_{k \neq l}^N \int_{-\infty}^{\infty} d\mathbf{r}_k \phi_k^* \phi_k \right) \quad (2.7)$$

where the integral $\prod_{k \neq l}^N \int_{-\infty}^{\infty} d\mathbf{r}_k \phi_k^* \phi_k = 1$ since ϕ is normalized. Therefore,

$$\int_{-\infty}^{\infty} \prod_{k=1}^N d\mathbf{r}_k \frac{i\hbar}{2} \theta_N^* \frac{\partial \theta_N}{\partial t} = \frac{i\hbar}{2} N \int_{-\infty}^{\infty} d\mathbf{r} \phi^*(\mathbf{r}, t) \cdot \frac{\partial \phi(\mathbf{r}, t)}{\partial t} \quad (2.8)$$

The second term in equation (2.5) is the complex conjugate of the first, hence:

$$\int_{-\infty}^{\infty} \prod_{k=1}^N d\mathbf{r}_k \frac{i\hbar}{2} \theta_N \frac{\partial \theta_N^*}{\partial t} = \frac{i\hbar}{2} N \int_{-\infty}^{\infty} d\mathbf{r} \phi(\mathbf{r}, t) \cdot \frac{\partial \phi^*(\mathbf{r}, t)}{\partial t} \quad (2.9)$$

The third term gives:

$$\int_{-\infty}^{\infty} \prod_{k=1}^N d\mathbf{r}_k \sum_{n=1}^N \frac{\hbar^2}{2m} |\nabla_n \theta_N|^2 = \frac{\hbar^2}{2m} N \int_{-\infty}^{\infty} d\mathbf{r} |\nabla \phi(\mathbf{r}, t)|^2 \quad (2.10)$$

The fourth term implies:

$$\int_{-\infty}^{\infty} \sum_{n=1}^N V(\mathbf{r}_n) |\theta_N|^2 = N \int_{-\infty}^{\infty} d\mathbf{r} V(\mathbf{r}) |\phi(\mathbf{r}, t)|^2 \quad (2.11)$$

Finally, the interaction term gives:

$$\int_{-\infty}^{\infty} \prod_{k=1}^N d\mathbf{r}_k \sum_{n=1}^N \sum_{i \neq n}^N \delta(\mathbf{r}_n - \mathbf{r}_i) |\theta_N|^2 = N(N-1) \int_{-\infty}^{\infty} d\mathbf{r} |\phi(\mathbf{r}, t)|^4 \quad (2.12)$$

Putting all these terms together yields:

$$L = N \int_{-\infty}^{\infty} d\mathbf{r} \left[\frac{\hbar}{2} \left(\phi^* \frac{\partial \phi}{\partial t} - \phi \frac{\partial \phi^*}{\partial t} \right) - \frac{\hbar^2}{2m} |\nabla \phi|^2 - V(\mathbf{r}) |\phi|^2 - \frac{g}{2} (N-1) |\phi|^4 \right] \quad (2.13)$$

The stationary state with respect to ϕ^* is obtained by setting $\frac{\partial L}{\partial \phi^*} = 0$, which implies:

$$N \int_{-\infty}^{\infty} d\mathbf{r} \left[\frac{i\hbar}{2} \frac{\partial \phi}{\partial t} - \frac{\hbar^2}{2m} \nabla^2 \phi - V(\mathbf{r})\phi - g(N-1)|\phi|^2\phi \right] = 0 \quad (2.14)$$

This leads to:

$$i\hbar \frac{\partial \phi}{\partial t} = -\frac{\hbar^2}{2m} \nabla^2 \phi + V(\mathbf{r})\phi + g(N-1)|\phi|^2\phi \quad (2.15)$$

The factor $N-1$ in the right-hand side ensures that the interaction term vanishes if $N=1$. However, in real BEC the number of atoms N is at least 10^5 , therefore $N-1$ can be replaced effectively with N . Thus the Gross-Pitaevskii equation can be written in its final form as:

$$i\hbar \frac{\partial \phi}{\partial t} = \left(-\frac{\hbar^2}{2m} \nabla^2 + V(\mathbf{r}) + gN|\phi|^2 \right) \phi \quad (2.16)$$

The equation was discovered independently by Gross and Pitaevskii in 1961. The total number of atoms and the energy of the system is given as:

$$N = \int_{-\infty}^{\infty} |\phi(\mathbf{r}, t)|^2 d\mathbf{r} \quad (2.17)$$

$$E = \int_{-\infty}^{\infty} \left[\frac{\hbar^2}{2m} |\nabla \psi|^2 + V(\mathbf{r})|\psi|^2 + \frac{1}{2} U_0 |\psi|^4 \right] d\mathbf{r} \quad (2.18)$$

where $U_0 = \frac{4\pi\hbar^2 a}{m}$, a is the atomic scattering length, m is the mass. The first term corresponds to the kinetic energy and the second and third terms correspond to the interaction potential energy.

2.4 Ground State of Trapped Boson

The ground state of the BEC can be obtained through variational calculation or through the Thomas-Fermi approximation which is approximately correct for BEC with large number of particles. Before looking at detailed mathematical derivation of the ground state, let's highlight some of its qualitative properties. We shall be considering the harmonic trap (although the formalism can be extended to other traps), ignore its anisotropic nature and take the potential to be of the form $V = \frac{m\omega_0^2 r^2}{2}$. If the spatial extent of the cloud is proportional to R , the potential and kinetic energy of the oscillator will be given respectively as $\frac{m\omega_0^2 R^2}{2}$ and $\frac{\hbar^2}{2mR^2}$ per particle. Let's consider the case where there is no interaction in the system, the Gross-Pitaevskii equation reduces to the usual Schrödinger equation and since from Heisenberg uncertainty principle a particle's momentum is of order $\frac{\hbar}{R}$. Thus the total energy varies as $\frac{1}{R}$ for small R and $\frac{1}{R^2}$ for large R and has a minimum when the kinetic and potential energy are equal. The corresponding value of the radius of the cloud is:

$$a_{\text{osc}} = \sqrt{\frac{\hbar}{m\omega_0}} \quad (2.19)$$

which is the characteristic quantum mechanical length for harmonic oscillator, a typical value we would expect from variational calculation. Let's consider the case where we have interaction between atoms of the BEC. The interaction in the system can either be attractive or repulsive depending on the atomic scattering length. When the atomic

scattering length is less than zero, the gas tends to increase its density at the center of the trap in order to lower its interaction energy. This is contrasted by the zero point kinetic energy which stabilizes the system. Hence, the energy of the system is similar to that of the non-interacting particles. However, if the number of particles grows too much beyond a critical value, N_{cr} , the kinetic energy is no longer able to avoid the collapse of the system, hence the system collapses. In a given system for a given trap, the N_{cr} is of the order $\frac{a_{osc}}{|a|}$. In a uniform gas where the quantum pressure is absent, the condensate is always unstable corresponding to a local minima of the energy functional [17] for different N . When N increases the depth of the local minimum decreases. Above N_{cr} the minimum no longer exists and the Gross-Pitaevskii equation has no solution. For a spherical trap this happens at $\frac{N_{cr}|a|}{a_{osc}} = 0.575$ [12]. For the axially symmetric trap with Li used in experiments at Rice University [17], the GP equation predicts $N \approx 1400$ and is consistent with recent experimental measurements [17]. A direct insight into the behaviour of the gas with attractive interaction can be obtained by means of variational approach based on a Gaussian function [12]. For a spherical trap one minimizes the energy [17] using the ansatz:

$$\phi(r) = \left(\frac{N}{w^3 a_{osc}^3 \pi^{3/2}} \right)^{1/2} \exp \left(-\frac{r^2}{2w^2 a_{osc}^2} \right) \quad (2.20)$$

where w is a dimensionless variational parameter which fixes the width of the condensate. One gets for the energy:

$$\frac{E(w)}{N \hbar \omega_{ho}} = \frac{3}{4} (w^{-2} + w^2) - \left(\frac{2}{\pi} \right)^{-1/2} \frac{N|a|}{a_{ho}} w^{-3} \quad (2.21)$$

A plot of the energy for several values of the parameter $\frac{N|a|}{a_{osc}}$ can be obtained. One clearly sees that the local minimum disappears when this parameter exceeds a critical value. It can also be shown that $w_{cr} = 5^{-1/4} \approx 0.671$. The stability of a condensate has been explored, for instance, by [18, 19, 20, 21]. For repulsive interactions, the limit $\frac{Na}{a_{osc}} \gg 1$ is of particular interest, since this condition is well satisfied by the parameters N , a , and a_{osc} used in most of the current experiments. With respect to the ground state, the effect of increasing the parameter $\frac{Na}{a_{osc}}$ is that the atoms are pushed outwards, the central density becomes flat, and the radius grows. As a consequence, the quantum pressure term in the Gross-Pitaevskii equation, proportional to $\nabla^2 \sqrt{n(r)}$, contributes significantly only near the boundaries and becomes less important with respect to the interaction energy. If quantum pressure is neglected, one obtains a density profile in the form:

$$n(r) = \phi^2(r) = g^{-1}[\mu - V_{ext}(r)] \quad (2.22)$$

in the region where $\mu > V_{ext}(r)$, and $n = 0$ outside.

2.5 The Variational Approximation

As introduced above, the variational method is a powerful approximation technique in quantum mechanics used to estimate the ground state energy and wavefunction of a system when an exact solution is not available. The central idea is to assume a trial wavefunction Ψ_{trial} , which depends on one or more variational parameters, and then minimize the expectation value of the Hamiltonian with respect to those parameters.

Mathematically, the variational principle states that for any normalized wavefunction Ψ_{trial} , the following inequality holds:

$$E_0 \leq \frac{\langle \Psi_{\text{trial}} | \hat{H} | \Psi_{\text{trial}} \rangle}{\langle \Psi_{\text{trial}} | \Psi_{\text{trial}} \rangle}, \quad (2.23)$$

where E_0 is the exact ground state energy and \hat{H} is the system Hamiltonian. The equality holds if and only if Ψ_{trial} is the exact ground state wavefunction. In practice, one chooses a trial wavefunction guided by the physical properties of the system (e.g., symmetry, boundary conditions, external potentials) and then optimizes the variational parameters to minimize the energy. This provides both an estimate of the ground state energy and insight into the approximate form of the ground state wavefunction. For Bose–Einstein condensates, the variational method is particularly useful because the Gross–Pitaevskii equation generally cannot be solved analytically except in simple cases. By choosing a physically motivated trial function (such as a Gaussian in a harmonic trap), one can extract important properties of the condensate, such as its size, shape, and chemical potential. If we consider a trial wave function [22, 23]:

$$\Psi(\mathbf{r}, t) = \psi_0(\mathbf{r}) \exp\left(-\frac{i\mu t}{\hbar}\right) \quad (2.24)$$

where ψ_0 is a function normalized to the number of atoms $N = \int |\psi_0| d\mathbf{r}$ and $\mu = \frac{\partial E}{\partial N}$ is the chemical potential, the time dependent Gross-Pitaevskii equation is given as:

$$i\hbar \frac{\partial \psi(\mathbf{r}, t)}{\partial t} = \left[-\frac{\hbar^2}{2m} \nabla^2 + V(\mathbf{r}) + g|\psi(\mathbf{r}, t)|^2 \right] \psi(\mathbf{r}, t) \quad (2.25)$$

Substituting (2.23) into (2.24), the first term on the left yields:

$$\frac{\partial \psi(\mathbf{r}, t)}{\partial t} = \frac{\partial}{\partial t} \left(\psi_0(\mathbf{r}) \exp\left(-\frac{i\mu t}{\hbar}\right) \right) = \frac{-i\mu}{\hbar} \psi_0(\mathbf{r}) \exp\left(-\frac{i\mu t}{\hbar}\right) \quad (2.26)$$

the first term on the right yields:

$$-\frac{\hbar^2}{2m} \nabla^2 \psi(\mathbf{r}, t) = -\frac{\hbar^2}{2m} \exp\left(-\frac{i\mu t}{\hbar}\right) \nabla^2 \psi_0(\mathbf{r}) \quad (2.27)$$

The second term on the right side yields:

$$|\psi(\mathbf{r}, t)|^2 = \psi(\mathbf{r}, t) \psi^*(\mathbf{r}, t) = \psi_0^*(\mathbf{r}) \exp\left(-\frac{i\mu t}{\hbar}\right) \psi_0(\mathbf{r}) \exp\left(\frac{i\mu t}{\hbar}\right) = |\psi_0(\mathbf{r})|^2 \quad (2.28)$$

Putting these together into (2.24):

$$\psi_0(\mathbf{r}) \mu = -\frac{\hbar^2}{2m} \nabla^2 \psi_0(\mathbf{r}) + V(\mathbf{r}) \psi_0(\mathbf{r}) + g|\psi_0|^2 \psi_0(\mathbf{r}) \quad (2.29)$$

$$\left(-\frac{\hbar^2}{2m} \nabla^2 + V(\mathbf{r}) + g|\psi_0|^2 - \mu \right) \psi_0(\mathbf{r}) = 0 \quad (2.30)$$

$g = 0$ implies that there is no interaction in the system and thus reduces the equation to the usual Schrödinger equation with potential V . To be more specific, if we consider an

external potential of the harmonic form, that is using a harmonic trap, we can find the ground state of the system, making assumptions that all bosons are in the single body state. In this state the ground solution ψ_0 is given as:

$$\psi_0 = \sqrt{N} \left(\frac{m\omega_m}{\pi\hbar} \right)^{3/4} \exp \left(-\frac{m}{2\hbar} (\omega_x x^2 + \omega_y y^2 + \omega_z z^2) \right) \quad (2.31)$$

where ω_m is the geometric mean of the confining frequencies mathematically $\omega_m = (\omega_x \cdot \omega_y \cdot \omega_z)^{1/3}$.

2.6 Thomas-Fermi Approximation

The Thomas-Fermi (TF) approximation is a simplification technique widely used in the study of Bose-Einstein condensates when the interatomic interaction energy greatly exceeds the kinetic energy contribution [16]. In this limit, the kinetic energy term in the Gross-Pitaevskii equation can be neglected, leading to a direct relationship between the condensate density and the external trapping potential. This approach is particularly valid for large condensates with strong repulsive interactions, where the healing length is much smaller than the system size. The resulting density profile, often referred to as the Thomas-Fermi profile, exhibits a parabolic shape in harmonic traps and allows for analytical determination of several key properties, such as the chemical potential and radius of the condensate.

To determine the ground-state energy of a Bose-Einstein condensate, one can employ the variational method using an educated guess for the trial wave function, such as a Gaussian, or apply the Thomas-Fermi approximation, which neglects the kinetic energy of the particles at temperatures close to absolute zero [14]. At finite temperatures, deviations from the Thomas-Fermi approximation become significant. While this approximation provides excellent results for systems with a very large number of particles, it becomes less accurate for condensates containing a moderate number of atoms. Considering the one-dimensional Gross-Pitaevskii equation [15, 16]:

$$-\frac{\hbar^2}{2m} \frac{\partial^2 \phi}{\partial x^2} + V(x)\phi(x, t) + g|\psi|^2\psi(x, t) = 0 \quad (2.32)$$

Applying the Thomas-Fermi approximation:

$$V(x)\psi + g|\psi|^2\psi = 0 \quad (2.33)$$

A solution to the wave function can thus be found to be:

$$\psi(x, t) = \sqrt{\frac{\mu - V_{\text{trap}}(x)}{U_0}} \quad \text{for } \mu > V_{\text{trap}} \quad (2.34)$$

If we let the trapping potential be that of simple Harmonic Potential trap and use the fact that the wave function is normalized, the Thomas-Fermi relationship between the condensate and the eigenvalue and the number of atoms in the system:

$$\mu = \left(\frac{15U_0}{64\pi\hbar\omega} \right)^{2/5} \left(\frac{2m\omega_*}{\hbar} \right)^{3/5} \quad (2.35)$$

where ω_* is the geometric mean of the trap given as:

$$\omega_* = (\omega_x \omega_y \omega_z)^{1/3} \quad (2.36)$$

We observe the dependence of the condensate energy on the number of atoms. For too large N limit, then $\mu \propto N^{2/5}$. The change in size of condensate with the number of atoms in this limit is also very slow. The extent of the wave function along each axis being:

$$r_i = \left(\frac{2\mu}{m\omega_i} \right)^{1/2} \propto N^{1/5} \quad \text{where } i \in \{x, y, z\} \quad (2.37)$$

2.7 Dimensional Reduction of the Gross-Pitaevskii Equation

For a Bose-Einstein condensate confined in a three-dimensional harmonic potential:

$$V(\mathbf{r}) = \frac{1}{2}m(\omega_x^2 x^2 + \omega_y^2 y^2 + \omega_z^2 z^2) \quad (2.38)$$

the geometry of the condensate is determined by the relative magnitudes of the trapping frequencies ω_i [14]. Three characteristic regimes emerge:

- **Isotropic trap** ($\omega_x = \omega_y \equiv \omega_r = \omega_z$): Produces a spherically symmetric condensate
- **Cigar-shaped trap** ($\omega_r > \omega_z$): Creates an axially elongated condensate
- **Pancake-shaped trap** ($\omega_z > \omega_r$): Yields a radially extended, disk-like condensate

In the strongly anisotropic limit where $\omega_z \gg \omega_r$ or $\omega_r \gg \omega_z$, the system undergoes dimensional reduction [25]:

- Quasi-2D system when $\omega_z \gg \omega_r$
- Quasi-1D system when $\omega_r \gg \omega_z$

These reduced dimensions exhibit unique quantum properties that have been extensively studied theoretically [26, 27] and realized experimentally using both magnetic [27] and optical trapping techniques [28].

2.7.1 Quasi-1D Reduction

For the cigar-shaped geometry ($\omega_r \gg \omega_z$), we employ the factorization ansatz:

$$\Psi(x, y, z, t) = \phi(x, t)\psi(y, z, t) \quad (2.39)$$

$$\psi(y, z, t) = \theta(y, z)e^{-i\mu_0 t/\hbar} \quad (2.40)$$

where μ_0 is the chemical potential and $\theta(y, z)$ satisfies the transverse ground state equation:

$$\left[-\frac{\hbar^2}{2m} \nabla_{\perp}^2 + \frac{1}{2}m\omega_r^2(y^2 + z^2) \right] \theta(y, z) = \mu_0 \theta(y, z) \quad (2.41)$$

Substituting into the Gross-Pitaevskii equation:

$$i\hbar \frac{\partial \Psi}{\partial t} = \left[-\frac{\hbar^2}{2m} \nabla^2 + V(\mathbf{r}) + g|\Psi|^2 \right] \Psi \quad (2.42)$$

we obtain after simplification:

$$i\hbar \theta(y, z) \frac{\partial \phi}{\partial t} = \left[-\frac{\hbar^2}{2m} \frac{\partial^2}{\partial x^2} + \frac{1}{2} m \omega_x^2 x^2 + g |\phi|^2 |\theta|^2 \right] \phi \theta \quad (2.43)$$

Multiplying by θ^* and integrating over the transverse coordinates yields the effective 1D GPE:

$$i\hbar \frac{\partial \phi}{\partial t} = \left[-\frac{\hbar^2}{2m} \frac{\partial^2}{\partial x^2} + \frac{1}{2} m \omega_x^2 x^2 + g_{1D} |\phi|^2 \right] \phi \quad (2.44)$$

with the effective 1D coupling constant:

$$g_{1D} = g \frac{C_2}{C_1} = \frac{2\hbar^2 a}{ma_\perp^2} \quad (2.45)$$

where $a_\perp = \sqrt{\hbar/m\omega_r}$ is the transverse oscillator length, and:

$$C_1 = \int |\theta(y, z)|^2 dy dz \quad (2.46)$$

$$C_2 = \int |\theta(y, z)|^4 dy dz \quad (2.47)$$

2.8 Hydrodynamic Formulation of the Gross–Pitaevskii Equation

The Gross–Pitaevskii equation (GPE) for a Bose–Einstein condensate (BEC) can be recast in a form analogous to the equations of classical fluid dynamics through the *Madelung transformation* [29]. This transformation separates the condensate wavefunction into a density field and a macroscopic phase, allowing the quantum fluid to be described in terms of familiar hydrodynamic quantities. Specifically, the condensate order parameter is written as

$$\psi(\mathbf{r}, t) = \sqrt{n(\mathbf{r}, t)} \exp[i S(\mathbf{r}, t)], \quad (2.48)$$

where $n(\mathbf{r}, t)$ denotes the condensate density and $S(\mathbf{r}, t)$ is a real-valued phase function related to the superfluid flow [13].

The local superfluid velocity field is obtained from the gradient of the phase:

$$\mathbf{v}(\mathbf{r}, t) = \frac{\hbar}{m} \nabla S(\mathbf{r}, t), \quad (2.49)$$

where m is the particle mass and \hbar the reduced Planck constant [14]. Substituting the Madelung form (2.48) into the time-dependent GPE and separating the real and imaginary parts yields two coupled equations. The imaginary part produces the continuity equation, expressing local conservation of mass:

$$\frac{\partial n}{\partial t} + \nabla \cdot (n \mathbf{v}) = 0, \quad (2.50)$$

which matches the classical mass conservation law [30]. The real part gives a quantum analogue of the Euler equation for an inviscid, compressible fluid:

$$m \frac{\partial \mathbf{v}}{\partial t} + \nabla \left(\mu + \frac{1}{2} mv^2 - \frac{\hbar^2}{2m\sqrt{n}} \nabla^2 \sqrt{n} \right) = 0, \quad (2.51)$$

where μ is the local chemical potential. The final term, proportional to \hbar^2 , is known as the *quantum pressure* term [31]. It has no analogue in classical hydrodynamics and arises from density gradients at the scale of the healing length, capturing dispersive effects that are crucial for phenomena such as quantum vortices and solitons. This hydrodynamic formulation provides a direct link between microscopic quantum dynamics and macroscopic fluid behaviour, making it a powerful tool for analysing superfluid flows and nonlinear excitations in Bose–Einstein condensates.

2.9 GPE in 1D with Harmonic Oscillator Potential

For N particles in a 1D harmonic trap, the wave function θ satisfies:

$$-\frac{\hbar^2}{2m} \frac{\partial^2 \theta}{\partial x^2} + \frac{1}{2} m\omega x^2 \theta + g|\theta|^2 \theta = E\theta \quad (2.52)$$

Using the rescaling:

$$x = \sqrt{\frac{\hbar}{m\omega}} \gamma \quad (2.53)$$

$$\theta = \left(\frac{m\omega}{\hbar} \right)^{1/4} \phi \quad (2.54)$$

$$g = \lambda \hbar \omega \sqrt{\frac{\hbar}{m\omega}} \quad (2.55)$$

we obtain the dimensionless form:

$$-\frac{1}{2} \frac{\partial^2 \phi}{\partial \gamma^2} + \frac{1}{2} \gamma^2 \phi + \lambda |\phi|^2 \phi = \frac{E}{\hbar\omega} \phi \quad (2.56)$$

Using a Gaussian ansatz:

$$\phi(\gamma) = \frac{1}{(b\pi)^{1/4}} \exp \left(-\frac{\gamma^2}{2b^2} \right) \quad (2.57)$$

the ground state energy is:

$$\frac{E}{\hbar\omega} = \frac{1}{4} \left(\frac{1}{b^2} + b^2 \right) + \frac{\lambda}{b\sqrt{2\pi}} \quad (2.58)$$

2.10 Vortices in Optics and Bose–Einstein Condensates

An *optical vortex* is a phase singularity in an optical field, corresponding to a point (or line, in three dimensions) of zero intensity around which the phase of the light wave

changes by an integer multiple of 2π [32, 33]. Such vortices arise when the light beam carries *orbital angular momentum* (OAM), which can be visualized as the wavefront twisting like a corkscrew around its axis of propagation. At the singularity core, the destructive interference of the helical wavefront leads to complete cancellation of intensity. In a transverse plane, an optical vortex typically appears as a bright ring surrounding a dark central region.

Each optical vortex is characterized by an integer *topological charge* l , defined as the number of 2π phase windings around the vortex core [34]. The magnitude of l determines the number of helical twists per wavelength, and thus the strength of the OAM carried by the beam. Higher topological charge corresponds to faster azimuthal phase rotation and can induce a greater torque on microscopic objects with electric dipole moments [35].

Optical vortices have diverse applications, particularly in optical communications, imaging, and quantum information processing. In quantum computing, they can be used to encode and store information in multiple OAM states, since in free space there is theoretically no upper limit to the topological charge [36]. This property offers the possibility of high-dimensional quantum information protocols and faster data manipulation. Optical vortices are also employed in optical tweezers to trap and manipulate micrometer-scale particles, such as biological cells [37]. Furthermore, the transfer of OAM between light and matter enables the study of quantum vortex dynamics in both linear and nonlinear regimes [38].

In superfluids such as Bose–Einstein condensates (BECs), quantized vortices exhibit unique properties and can be generated through a variety of mechanisms. In BECs with repulsive interactions, vortices are topologically stable, higher-dimensional nonlinear excitations that can be investigated both experimentally and theoretically [39, 40]. They may be generated in condensates of alkali atoms such as ^{87}Rb by rotating the condensate above a critical angular velocity [41, 42]. Another method involves splitting a BEC into several spatial fragments and then allowing them to interfere upon recombination, producing vortex-antivortex pairs [43].

In multi-component (spinor) BECs, additional vortex transfer phenomena can occur. For instance, in a two-component condensate where one component contains a vortex lattice, experiments have demonstrated the complete transfer of vortices to the second component through coherent coupling [44]. This capability allows controlled transfer of angular momentum and population between components, which can be exploited to engineer complex vortex configurations.

2.11 Bright Solitons in Nonlinear Dispersive Media

It is well established that the interplay between nonlinearity and dispersion can give rise to localized wave packets that propagate without distortion [45, 46]. In Bose–Einstein condensates (BECs), when the interatomic interaction is attractive (i.e., the s -wave scattering length is negative), the system supports *bright solitons* [47, 48]. These solitary waves maintain their shape due to a balance between nonlinear self-focusing and disper-

sive spreading.

In integrable systems, bright solitons exhibit *elastic* collisions, meaning that their shape, velocity, and amplitude remain unchanged after interaction. However, many realistic physical systems are *nonintegrable*, and although they may support stationary or moving localized wave solutions, collisions between them are generally inelastic, indicating that they are not true solitons in the strict mathematical sense [49]. Nonetheless, such solitary waves are often referred to as “solitons” in the literature due to their stability and particle-like behavior.

Bright solitons occur more frequently than their counterpart, the *dark soliton*, in certain physical settings. A classical hydrodynamic example is the solitary wave (hump) propagating in shallow water [50]. Beyond fluid dynamics, bright solitons are found in optical fibers [51], plasma systems [52], macromolecules [53], acoustics [54], and excitonic systems [55]. In nonlinear optics, the nondispersing nature of optical bright solitons makes them highly valuable for applications in optical communications and photonics [56, 46]. A notable example is the *gap soliton*, which arises in a repulsive BEC confined in an optical lattice. Here, the periodic potential modifies the dispersion relation via the band-gap structure, enabling the formation of bright solitons despite the repulsive interaction [57].

2.12 Dark Solitons in Bose–Einstein Condensates

Dark solitons arise in systems with effective repulsive interactions. They are characterized by a localized dip in the background density and an associated phase slip, and are often regarded as one-dimensional analogues of vortices [58]. Compared to their bright soliton counterparts, dark solitons are relatively rare and have been experimentally realized in only a limited number of systems. In atomic Bose–Einstein condensates (BECs) with repulsive interactions, dark solitons have been generated using *phase imprinting* techniques [59, 60, 61] and through density perturbations [62]. They have also been theoretically predicted to form during the collision of two condensates [63, 64] or in response to a time-dependent obstacle moving through the condensate [65, 66, 67].

In realistic systems, the presence of dissipation leads to the decay of dark solitons at arbitrary positions within the condensate. In harmonically trapped, dilute BECs, dark solitons typically undergo oscillatory motion, and their interaction with thermal excitations at the density node results in a gradual reduction of the density contrast and an increase in oscillation amplitude [68]. Since the dark soliton is a strictly one-dimensional solution of the nonlinear Schrödinger equation, it is inherently prone to *transverse instability* when embedded in higher dimensions. In three-dimensional geometries with weak transverse confinement, this instability manifests as the well-known *snake instability* [69, 70, 61]. Similar transverse instabilities have been observed experimentally in two-dimensional optical media [71, 72].

2.13 Dynamical Instabilities and Excitations in Vortices and Dark Solitons

Dynamical instabilities in vortices and dark solitons generally lead to the emission of sound waves [73, 74]. In dilute Bose–Einstein condensates (BECs), the presence of external trapping potentials confines the condensate to a finite size, which in turn restricts the allowed excitations within the system [75]. Consequently, a vortex or dark soliton in a typical BEC coexists with other excitations and collective modes. In this context, the vortex or soliton is not strictly a pure, unperturbed topological structure in the mathematical sense, but rather represents a spatial region in which the vortex or soliton is embedded along with these coexisting excitations within the Gross–Pitaevskii framework [13]. Nevertheless, this does not pose a significant issue, as experimental measurements probe precisely this combined behavior of the vortex or soliton and its surrounding local excitations [61, 76].

Chapter 3

Numerical Methods

3.1 Numerical Method

Numerical methods are essential for solving problems that lack analytical solutions. In this section, we present a time-splitting spectral method tailored for the one-dimensional Gross–Pitaevskii equation (GPE) with periodic boundary conditions. Specifically, we employ the Strang splitting technique to handle the nonlinear terms effectively. Consider the 1D GPE with a harmonic potential:

$$i\frac{\partial\phi}{\partial t} = -\frac{1}{2}\frac{\partial^2\phi}{\partial x^2} + \frac{x^2}{2}\phi(x, t) + \kappa|\phi(x, t)|^2\phi(x, t), \quad (3.1)$$

subject to the initial condition:

$$\phi(x, 0) = \phi_0(x), \quad a < x < b, \quad (3.2)$$

and periodic boundary conditions:

$$\phi(a, t) = \phi(b, t), \quad \frac{\partial\phi}{\partial x}(a, t) = \frac{\partial\phi}{\partial x}(b, t), \quad t > 0. \quad (3.3)$$

We discretize the spatial domain with mesh size $h = \Delta x = \frac{b-a}{M}$, where M is an even positive integer, and the temporal domain with time steps $t_n = n\Delta t$. The spatial grid points are:

$$x_j = a + jh, \quad j = 0, 1, \dots, M, \quad (3.4)$$

and the temporal grid points are:

$$t_n = n\Delta t, \quad n = 0, 1, 2, \dots \quad (3.5)$$

Let θ_j^n denote the numerical approximation of $\phi(x_j, t_n)$ at the grid point (x_j, t_n) , and let ϕ^n represent the vector of all spatial components at time t_n , i.e.,

$$\phi^n = (\phi_0^n, \phi_1^n, \dots, \phi_M^n)^T. \quad (3.6)$$

The Strang splitting method decomposes the evolution operator into linear and nonlinear parts, allowing for efficient computation. This approach is particularly advantageous for the GPE, as it preserves key properties such as mass and energy conservation, and is second-order accurate in time and spectrally accurate in space [77, 78, 79].

3.2 Lie Splitting Method (LSM)

The Lie splitting method decomposes the time evolution of the Schrödinger equation from $t = t_n$ to $t = t_{n+1}$ into two sequential steps. First, the linear kinetic term is solved:

$$i \frac{\partial \phi}{\partial t} = -\frac{1}{2} \frac{\partial^2 \phi}{\partial x^2}, \quad (3.7)$$

followed by the nonlinear potential term:

$$i \frac{\partial \phi}{\partial t} = \frac{x^2}{2} \phi(x, t) + \kappa_1 |\phi(x, t)|^2 \phi(x, t). \quad (3.8)$$

Equation (4.1) is discretized in space using the spectral method and integrated exactly in time, whereas (4.2) is an ordinary differential equation with a known exact solution. The splitting procedure is expressed as:

$$\theta_j^* = \frac{1}{M} \sum_{l=-M/2}^{M/2-1} \exp\left(-\frac{i\Delta t \mu_l^2}{2}\right) \hat{\theta}_l^n \exp[i\mu_l(x_j - a)], \quad (3.9)$$

for $j = 0, 1, \dots, M - 1$, and

$$\theta_j^{n+1} = \exp[-iV(x_j)\Delta t] \theta_j^*, \quad (3.10)$$

where $\hat{\theta}_l^n$ are the Fourier coefficients of θ^n :

$$\hat{\theta}_l^n = \sum_{j=0}^{M-1} \theta_j^n \exp[-i\mu_l(x_j - a)], \quad \mu_l = \frac{2\pi l}{b-a}, \quad l = -\frac{M}{2}, \dots, \frac{M}{2} - 1, \quad (3.11)$$

with initial condition $\theta_j^0 = \phi_0(x_j)$. The primary source of time discretization error in this method arises from the splitting itself, which is first-order in Δt [77, 78].

3.3 Strang Splitting Spectral Method (SSM)

The Strang splitting method improves accuracy by symmetrically applying the linear and nonlinear steps:

1. Solve the linear part over half a time step $[t_n, t_{n+0.5}]$ using the initial condition.
2. Solve the nonlinear part over a full time step $[t_n, t_{n+1}]$ using the solution from step 1.
3. Solve the linear part again over half a time step $[t_{n+0.5}, t_{n+1}]$ using the solution from step 2.

In discretized form, the method is written as:

$$\theta_j^* = \exp\left[-iV(x_j) \frac{\Delta t}{2}\right] \theta_j^n, \quad (3.12)$$

$$\theta_j^{**} = \exp\left[-i\kappa_1 |\theta_j^*|^2 \Delta t\right] \theta_j^*, \quad (3.13)$$

$$\theta_j^{n+1} = \exp \left[-iV(x_j) \frac{\Delta t}{2} \right] \theta_j^{**}. \quad (3.14)$$

The Fourier coefficients of θ^* are given by:

$$\hat{\theta}_l^* = \sum_{j=0}^{M-1} \theta_j^* \exp[-i\mu_l(x_j - a)], \quad l = -\frac{M}{2}, \dots, \frac{M}{2} - 1. \quad (3.15)$$

The overall time discretization error in Strang splitting is second-order in Δt [79, 77]. For a constant potential $V(x) = V$, both Lie and Strang splitting steps can be combined as:

$$\theta_j^n = \frac{1}{M} \sum_{l=-M/2}^{M/2-1} \exp \left[-i \left(\frac{\mu_l^2}{2} + V \right) t_n \right] \hat{\theta}_l^0 \exp[i\mu_l(x_j - a)], \quad (3.16)$$

$$\hat{\theta}_l^0 = \sum_{j=0}^{M-1} \theta_j^0 \exp[-i\mu_l(x_j - a)], \quad l = -\frac{M}{2}, \dots, \frac{M}{2} - 1. \quad (3.17)$$

In this scenario, the second-order space derivative is discretized spectrally and the resulting ODE system is solved exactly, eliminating time discretization error while retaining spectral accuracy in space [78].

3.4 Error Estimates

Error estimates are provided for the Strang splitting method, although they are not rigorously proved, as this method is implemented in our research. The stability of both the Lie splitting method and the Strang splitting method is established and proved, and the splitting of both methods is also justified [79].

Let $\mathbf{P} = (p_0, \dots, p_{M-1})^T$. We define the L^2 norm and the discrete l^2 norm on the interval (a, b) as

$$\|P\|_{L^2} = \sqrt{\int_a^b |P(x)|^2 dx}, \quad \|P\|_{l^2} = \sqrt{\frac{b-a}{M} \sum_{j=0}^{M-1} |\theta_j|^2}. \quad (3.18)$$

We aim to show that the time-splitting spectral scheme and the Lie splitting spectral scheme are unconditionally stable, i.e., stable for any mesh size h and time step Δt :

$$\|\mathbf{P}^n\|_{l^2} = \|\theta^0\|_{l^2}, \quad n = 1, 2, \dots, \quad (3.19)$$

and consequently,

$$\|P_I^n\|_{L^2} = \|\theta^0\|_{L^2}, \quad n = 1, 2, \dots \quad (3.20)$$

where P_I^n denotes the trigonometric polynomial interpolating $(x_0, \theta_0^n), (x_1, \theta_1^n), \dots, (x_{M-1}, \theta_{M-1}^n)$.

Proof. We first recall the standard Fourier identities (to be completed):

$$\sum_{j=0}^{M-1} \exp(\dots) \quad (3.21)$$

From equations (3.1)–(3.3), we have:

$$\frac{1}{b-a} \|\theta^{n+1}\|_{L^2}^2 = \frac{1}{M} \sum_{j=0}^{M-1} |\theta_j^{n+1}|^2 = \frac{1}{M} \sum_{j=0}^{M-1} |\exp(-iV(x_j)\Delta t) \theta_j^*|^2, \quad (3.22)$$

$$\frac{1}{b-a} \|\theta^{n+1}\|_{L^2}^2 = \frac{1}{M} \sum_{j=0}^{M-1} |\theta_j^*|^2 = \frac{1}{M} \sum_{j=0}^{M-1} \left| \frac{1}{M} \sum_{l=-M/2}^{M/2-1} \exp\left(-\frac{i\Delta t \mu_l^2}{2}\right) \hat{\theta}_l^n \exp(i\mu_l(x_j - a)) \right|^2, \quad (3.23)$$

$$\frac{1}{b-a} \|\theta^{n+1}\|_{L^2}^2 = \frac{1}{M} \sum_{j=0}^{M-1} |\theta_j^n|^2 = \frac{1}{b-a} \|\theta^n\|_{L^2}^2. \quad (3.24)$$

For the Strang splitting method, using the previous assumptions, we obtain:

$$\frac{1}{b-a} \|\theta^{n+1}\|_{L^2}^2 = \frac{1}{M} \sum_{j=0}^{M-1} |\theta_j^{n+1}|^2 = \frac{1}{M} \sum_{j=0}^{M-1} \left| \exp\left(-\frac{iV(x_j)\Delta t}{2}\right) \theta_j^{**} \right|^2 \quad (3.25)$$

$$= \frac{1}{M} \sum_{j=0}^{M-1} \left| \frac{1}{M} \sum_{l=-M/2}^{M/2-1} \exp\left(-\frac{i\Delta t \mu_l^2}{2}\right) \hat{\theta}_l^* \exp(i\mu_l(x_j - a)) \right|^2 \quad (3.26)$$

$$= \frac{1}{M^2} \sum_{l=-M/2}^{M/2-1} \left| \exp\left(-\frac{i\Delta t \mu_l^2}{2}\right) \hat{\theta}_l^* \right|^2 \quad (3.27)$$

$$= \frac{1}{M^2} \sum_{l=-M/2}^{M/2-1} \left| \sum_{j=0}^{M-1} \theta_j^* \exp(-i\mu_l(x_j - a)) \right|^2 \quad (3.28)$$

$$= \frac{1}{M} \sum_{j=0}^{M-1} |\theta_j^n|^2 = \frac{1}{b-a} \|\theta^n\|_{L^2}^2. \quad (3.29)$$

Thus, unconditional stability is proven for both the Lie splitting and Strang splitting methods. To derive the error estimate, we assume that the initial condition (the initial wave function in our case) θ^0 is a positive constant C_∞ on \mathbb{R} and periodic with period $b-a$. Furthermore, we assume that positive constants $C_m > 0$ exist for every integer $m \geq 0$ such that: (A)

$$\left\| \frac{d^m}{dx^m} \phi_0 \right\|_{L^2(a,b)} \leq C_m. \quad (3.30)$$

3.5 Error Analysis for Constant Potential

For a constant potential $V(x) \equiv V$, both the Lie–Trotter and Strang splitting schemes reduce to the same update (see (3.17)). Let $\{\theta_j^n\}_{j=0}^{M-1}$ be the grid values produced by (3.12) under assumption (A), and let θ_I^n denote their trigonometric interpolant. Let θ be the exact solution of (3.1). If V is constant, then for any integer $m \geq 1$ there exist constants $D > 0$ (depending only on $b-a$) and $C_m > 0$ (depending on m and the regularity of the solution) such that

$$\|\theta_I^n - \theta(t_n)\|_{L^2(a,b)} \leq D C_m \left(\frac{h}{b-a} \right)^m. \quad (3.31)$$

Moreover, from the trigonometric interpolation, one obtains:

$$\|\theta_I^0 - \theta^0\|_{L^2(a,b)} \leq D \left(\frac{h}{b-a} \right)^m \left\| \frac{d^m}{dx^m} \theta^0 \right\|_{L^2(a,b)} \leq D C_m \left(\frac{h}{b-a} \right)^m, \quad (3.32)$$

for all $m \geq 1$, where $D > 0$ depends only on the length $(b-a)$. Since θ_I^n evolves, between time steps, according to the exact solution of (3.1) with periodic boundary conditions and initial datum θ_I^0 at $t = t_n$, and since the Schrödinger flow defines a unitary group on $L^2(a, b)$, the estimate (3.31) follows directly from (3.32).

Chapter 4

Results and Discussion

4.1 Introduction

Transport phenomena play a central role in a wide range of problems in physics, chemistry, and biology. A particularly intriguing example is the *ratchet effect*, in which a net directed current of particles is generated in a periodic structure without the presence of a net biasing force [80, 81]. This concept originates from the pioneering works of Smoluchowski and Feynman, initially motivated by the study of molecular motors in biological systems [82]. Over the past decades, ratchet models have found numerous applications [83], especially in systems where the particle mass plays a significant role [84]. In such cases, the dynamics can become considerably more complex, with phenomena such as chaotic motion and current reversals emerging.

In the present work, we aim to develop a directed transport model for particles diffusing in a ratchet potential. In particular, we consider a Bose–Einstein condensate (BEC) subjected to a time-periodically modulated optical ratchet potential. The dynamics of such a condensate are governed by the mean-field Gross–Pitaevskii equation (GPE), which we solve numerically using the split operator method. While numerous theoretical and experimental studies have investigated BECs in symmetric ratchet potentials [85], here we focus on an *asymmetric* ratchet configuration. Within this framework, we compute physical observables such as the atomic current, the condensate energy, and the fraction of non-condensate particles [86].

4.2 Results Presentation

The Grosspitaevskii equation is a very useful tool in investigating the dynamics of Bose Einstein Condensate. Here we start by analysing the GPE and the various attached terms. The time-dependent Gross–Pitaevskii equation (GPE) is given by

$$i\hbar \frac{\partial \Psi(\mathbf{r}, t)}{\partial t} = \left(-\frac{\hbar^2}{2m} \nabla^2 + V(\mathbf{r}) + g|\Psi(\mathbf{r}, t)|^2 \right) \Psi(\mathbf{r}, t), \quad (4.1)$$

where:

- $\Psi(\mathbf{r}, t)$ is the macroscopic wavefunction of the Bose–Einstein condensate (BEC), normalized as

$$\int |\Psi(\mathbf{r}, t)|^2 d^3r = N,$$

with N being the number of particles.

- $i\hbar \frac{\partial \Psi}{\partial t}$ describes the time evolution of the condensate.
- The first term on the right-hand side,

$$-\frac{\hbar^2}{2m} \nabla^2,$$

represents the kinetic energy of the particles, where ∇^2 is the Laplacian operator.

- $V(\mathbf{r})$ is the external trapping potential (in our case we would be considering the ratchet potential modulated in time) that confines the condensate.
- The nonlinear term,

$$g|\Psi(\mathbf{r}, t)|^2,$$

accounts for mean-field interactions between atoms. The coupling constant g is given by

$$g = \frac{4\pi\hbar^2 a_s}{m},$$

where a_s is the s -wave scattering length. For $a_s > 0$, interactions are repulsive and for $a_s < 0$, they are attractive.

Physically, $|\Psi(\mathbf{r}, t)|^2$ corresponds to the particle density, and the phase of Ψ determines the superfluid velocity via

$$\mathbf{v} = \frac{\hbar}{m} \nabla \theta,$$

where θ is the phase of Ψ . To study the dynamics of BEC via the GPE equation we would be considering two regimes, one where the external or trapping potential is zero and secondly where the external trapping potential is in the form of a ratchet potential modulated in time.

4.2.1 GPE Equation with external trapping potential $\mathbf{V} = 0$.

Let us consider the GPE equation of the form where $\mathbf{V} = 0$:

$$iQ_t + aQ_{xx} - b_1|Q|Q + b_2|Q|^2Q = 0, \quad (4.2)$$

$Q(x, t)$ is the macroscopic wavefunction of the condensate and $|Q|^2$ represents the atomic density. The terms have the following physical interpretations:

- iQ_t : Governs the time evolution of the condensate wavefunction.
- aQ_{xx} : The kinetic energy term associated with quantum pressure and dispersion effects.
- $-b_1|Q|Q$: Represents the contribution from *two-body interactions*. The parameter b_1 determines:
 - $b_1 > 0$: effective repulsive two-body interaction.
 - $b_1 < 0$: effective attractive two-body interaction.

- $+b_2|Q|^2Q$: Represents the contribution from *three-body interactions* or higher-order mean-field effects. The parameter b_2 determines:
 - $b_2 > 0$: additional repulsion at high densities (stabilizing effect).
 - $b_2 < 0$: effective attraction at high densities (possible condensate collapse).

We see that in this case the atoms are not confined by an external potential, thus are free to expand in space. However, due to balancing interaction between the various nonlinear terms, the atoms can be assumed to be confined and move uniformly in space and time as would be later described by our results. The next section, we would explore the dynamics of BEC where the external trapping potential $V=0$.

Bright Soliton Solution via Modified Ansatz Method

1. Governing Equation

In the context of a Bose–Einstein condensate (BEC), the Quartic–Cubic Nonlinear Schrödinger Equation (QC-NLSE) can be expressed as:

$$iQ_t + aQ_{xx} - b_1|Q|Q + b_2|Q|^2Q = 0 \quad (4.3)$$

We assume a solution of the form:

$$Q(x, t) = \Phi(x, t)e^{iP(x, t)}, \quad P(x, t) = -kx + \Omega t + \Theta \quad (4.4)$$

where $\Phi(x, t)$ is the amplitude and $P(x, t)$ is the phase. To solve the schrodinger equation avoiding singularities, we propose a solution of the form;

$$\Phi(x, t) = A_1(M_1 + N_1 \operatorname{sech}^{p_1}[B_1(x - v_1 t)]) \quad (4.5)$$

where $\tau_1 = B_1(x - v_1 t)$. We obtain the following derivation:

$$\Phi_t = A_1 N_1 p_1 v_1 B_1 \operatorname{sech}^{p_1} \tau_1 \tanh \tau_1 \quad (4.6)$$

$$\Phi_x = -A_1 N_1 p_1 B_1 \operatorname{sech}^{p_1} \tau_1 \tanh \tau_1 \quad (4.7)$$

$$\Phi_{xx} = -A_1 N_1 B_1^2 p_1 [(p_1 + 1) \operatorname{sech}^{p_1+2} \tau_1 - p_1 \operatorname{sech}^{p_1} \tau_1] \quad (4.8)$$

Substituting into the amplitude equation(4.3) yields:

$$v_1 = -2ak \quad (4.9)$$

$$\begin{aligned} & (\Omega - ak^2 - b_1 A_1 M_1 + b_2 A_1^2 M_1^2) A_1 M_1 \\ & + (\Omega + ap_1^2 B_1^2 - ak^2 - 2b_1 A_1 M_1 + 3b_2 A_1^2 M_1^2) A_1 N_1 \operatorname{sech}^{p_1} \tau_1 \\ & - a A_1 N_1 p_1 (p_1 + 1) B_1^2 \operatorname{sech}^{p_1+2} \tau_1 \\ & + (3b_2 A_1^3 M_1 N_1^2 - b_1 A_1^2 N_1^2) \operatorname{sech}^{2p_1} \tau_1 \\ & + b_2 A_1^3 N_1^3 \operatorname{sech}^{3p_1} \tau_1 = 0 \end{aligned} \quad (4.10)$$

Equating the highest exponents:

$$2p_1 = p_1 + 2 \implies p_1 = 2 \quad \text{or} \quad p_1 + 2 = 3p_1 \implies p_1 = 1 \quad (4.11)$$

Only $p_1 = 1$ yields stable solutions (the $p_1 = 2$ case produces singularity problems). Setting coefficients of $\text{sech}^n \tau_1$ terms to zero gives:

$$\Omega - ak^2 - b_1 A_1 M_1 + b_2 A_1^2 M_1^2 = 0 \quad (4.12)$$

$$-2aB_1^2 + b_2 A_1^2 N_1^2 = 0 \quad (4.13)$$

$$3b_2 A_1 M_1 - b_1 = 0 \quad (4.14)$$

$$\Omega + ak^2 + aB_1^2 - 2b_1 A_1 M_1 + 3b_2 A_1^2 M_1^2 = 0 \quad (4.15)$$

From Eq. (4.12 - 4.15), we obtain:

$$A_1 M_1 = \frac{b_1}{3b_2} \quad (4.16)$$

$$\Omega = ak^2 + \frac{2b_1^2}{9b_2} \quad (4.17)$$

$$A_1 N_1 = \pm \sqrt{2 \left(\frac{7b_1^2}{9b_2^2} - \frac{ak^2}{b_2} \right)} \quad (4.18)$$

$$B_1 = \pm \sqrt{\frac{7b_1^2}{9ab_2} - 2k^2} \quad (4.19)$$

The complete solution depicting the bright soliton is:

$$Q(x, t) = A_1 \left(\frac{b_1}{3b_2} + N_1 \text{sech} [B_1(x + 2akt)] \right) e^{i(-kx + \Omega t + \Theta)} \quad (4.20)$$

Hence the bright soliton solution of Eq. (1) is obtained. Figure 1 shows the propagation of a prototypical bright soliton, at velocity $v_1 = -ak$, depicted for specific values of the parameters fulfilling the conditions for existence of B_1 and $A_1 N_1$ that requires:

$$\frac{7b_1^2}{9b_2^2} - \frac{ak^2}{b_2} \geq 0, \quad \text{with } a/b_2 > 0; \quad (4.21)$$

that is, a and b_2 are nonzero real numbers of the same sign. Here $a = 20/9$, $b_1 = 1$, $b_2 = 2$, and $k = 1$, thereby imposing the velocity $v_1 = -20/9$. In a relatively short time, one can clearly appreciate the distance traveled by the soliton. Negative time means propagation backward. We further explored this propagation by increasing the soliton velocity. It turns out that the bright solitons are affected by velocity for any set of chosen parameters. When $v_1 \gg 1$ (high velocity), the soliton becomes unstable or nonexistent.

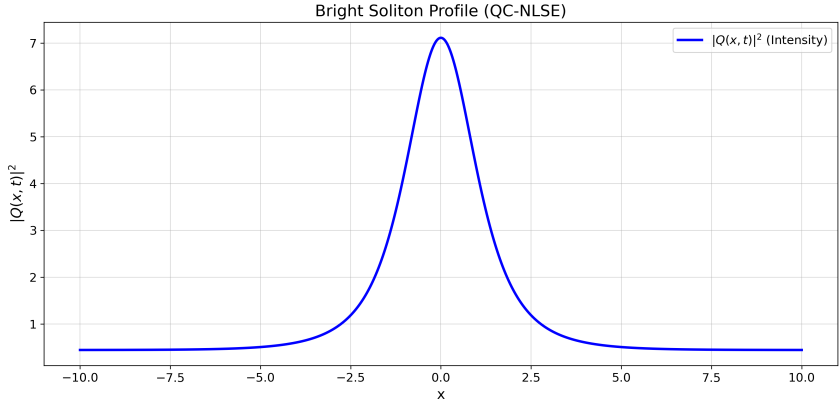


Figure 4.1: Initial condensate density profile $|\psi(x, 0)|^2$ of the bright soliton along the spatial coordinate x at $t = 0$. The soliton is localized around $x = 0$ and normalized according to $\int |\psi(x, 0)|^2 dx = 1$.

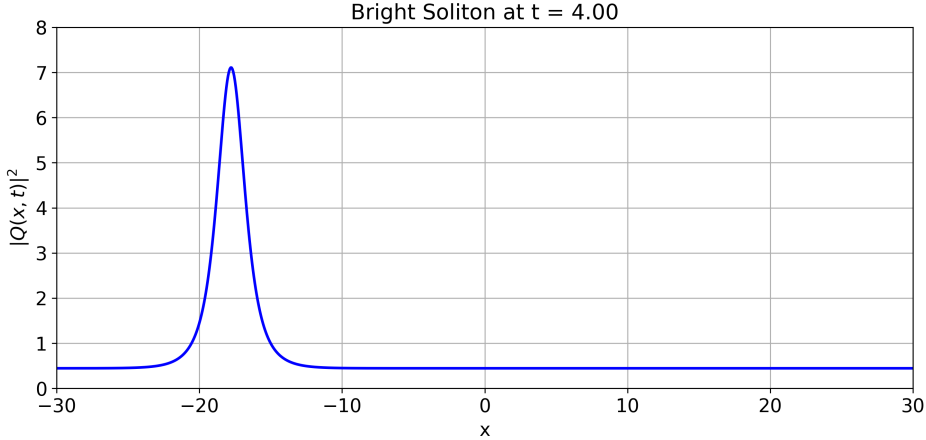


Figure 4.2: Space–time evolution of the condensate density at $t = 4.0$. The bright soliton has propagated in the negative x -direction while maintaining its shape and moving at a constant velocity. The observed stability arises from the balance between dispersion and the nonlinear interaction term in the Gross–Pitaevskii equation.

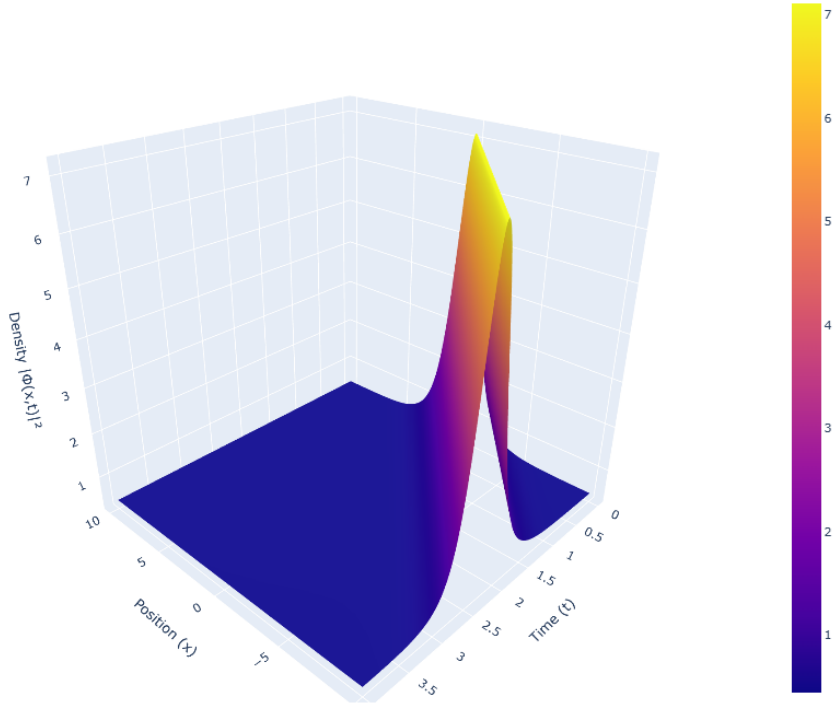


Figure 4.3: 3D visualization of a bright soliton: the localized wave packet maintains its shape while propagating in time due to a balance between dispersion and non-linearity.

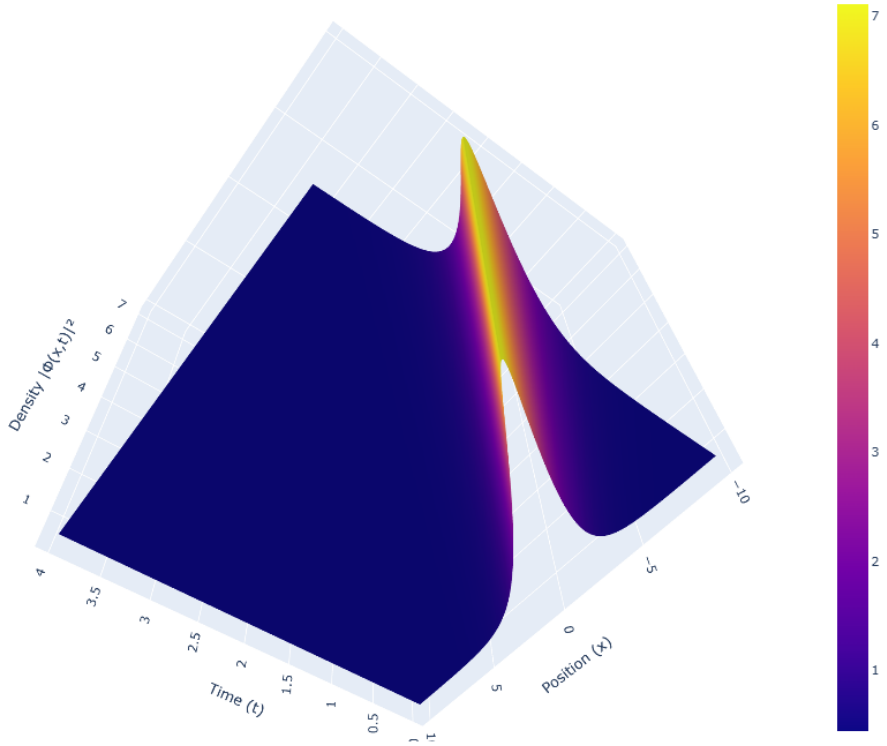


Figure 4.4: Three-dimensional view of the condensate density from an alternative perspective, illustrating the evolution of the condensate.

We observe that the bright soliton is a localised condensate pulse that propagates through space without spreading, moving at a constant velocity and maintaining constant shape and amplitude. We see from the density plot that the soliton moves in the negative x direction. The interplay between the dispersive and non-linear interaction terms tends to stabilize the atoms as they propagate through space.

4.2.2 Dark Soliton Solution Derivation

To explore the dynamics of the dark soliton we employ the modified ansatz given as:

$$\Phi(x, t) = A_2 \left(M_2 + N_2 \tanh^{p_2} (B_2(x - v_2 t)) \right), \quad (4.22)$$

where A_2 is a scaling constant, M_2 and N_2 are parameters associated with the soliton amplitude and shift, B_2 is the inverse width, v_2 is the soliton velocity, and p_2 is an exponent to be determined. The derivatives of the ansatz are computed as:

$$\Phi_t = -A_2 N_2 B_2 v_2 p_2 \left(\tanh^{p_2-1} \tau_2 - \tanh^{p_2+1} \tau_2 \right), \quad (4.23)$$

$$\Phi_x = A_2 N_2 p_2 B_2 \left(\tanh^{p_2-1} \tau_2 - \tanh^{p_2+1} \tau_2 \right), \quad (4.24)$$

$$\Phi_{xx} = A_2 N_2 p_2 B_2^2 \left((p_2 - 1) \tanh^{p_2-2} \tau_2 - 2p_2 \tanh^{p_2} \tau_2 + (p_2 + 1) \tanh^{p_2+2} \tau_2 \right), \quad (4.25)$$

where $\tau_2 = B_2(x - v_2 t)$. Substituting Eqs. (4.23 - 4.25) into the amplitude equation (4.3) and collecting like powers of $\tanh(\tau_2)$ yields:

$$\begin{aligned} & (\Omega - ak^2 - b_1 A_2 M_2 + b_2 A_2^2 M_2^2) A_2 M_2 \\ & + (\Omega - 2ap_2^2 B_2^2 - ak^2 - 2b_1 A_2 M_2 + 3b_2 A_2^2 M_2^2) A_2 N_2 \tanh^{p_2} \tau_2 \\ & + a A_2 N_2 B_2^2 p_2 (p_2 - 1) \tanh^{p_2-1} \tau_2 + a A_2 N_2 B_2^2 p_2 (p_2 + 1) \tanh^{p_2+2} \tau_2 \\ & + (b_1 + 3b_2 A_2 M_2) A_2^2 N_2^2 \tanh^{2p_2} \tau_2 + b_2 A_2^3 N_2^3 \tanh^{3p_2} \tau_2 = 0. \end{aligned} \quad (4.26)$$

Balancing the highest powers, $p_2 + 2$ and $2p_2$ or $p_2 + 2$ and $3p_2$, gives:

$$p_2 = 1 \quad (\text{since } p_2 = 2 \text{ leads to singularity}). \quad (4.27)$$

With $p_2 = 1$, Eq. (4.26) reduces to a polynomial in $\tanh(\tau_2)$. Setting the coefficients of $\tanh^n \tau_2$ to zero yields:

$$\Omega - ak^2 - b_1 A_2 M_2 + b_2 A_2^2 M_2^2 = 0, \quad (4.28)$$

$$\Omega - 2aB_2^2 - ak^2 - 2b_1 A_2 M_2 + 3b_2 A_2^2 M_2^2 = 0, \quad (4.29)$$

$$2aB_2^2 + b_2 A_2^2 N_2^2 = 0, \quad (4.30)$$

$$b_1 + 3b_2 A_2 M_2 = 0. \quad (4.31)$$

Solving Eqs. (4.28)–(4.31) gives:

$$A_2 M_2 = -\frac{b_1}{3b_2}, \quad (4.32)$$

$$\Omega = ak^2 - \frac{4}{9} \frac{b_1^2}{b_2}, \quad (4.33)$$

$$B_2 = \pm \frac{1}{\sqrt{2}} \left(\frac{5}{9} \frac{b_1^2}{ab_2} - k^2 \right)^{1/2}, \quad (4.34)$$

$$A_2 N_2 = \pm \left(\frac{a}{b_2} \left(\frac{5}{9} \frac{b_1^2}{ab_2} - k^2 \right) \right)^{1/2}. \quad (4.35)$$

The soliton velocity is given by:

$$v_2 = -2ak. \quad (4.36)$$

Finally, substituting these parameter values into Eq. (4.22) provides the explicit form of the dark soliton solution. The dark soliton solution to the Quartic-Cubic Nonlinear Schrödinger Equation is obtained as:

$$\Phi(x, t) = A_2 \left(M_2 + N_2 \tanh(B_2(x - v_2 t)) \right), \quad (4.37)$$

where the parameters are given by:

$$A_2 M_2 = -\frac{b_1}{3b_2}, \quad (4.38)$$

$$\Omega = ak^2 - \frac{4}{9} \frac{b_1^2}{b_2}, \quad (4.39)$$

$$B_2 = \pm \frac{1}{\sqrt{2}} \left(\frac{5}{9} \frac{b_1^2}{ab_2} - k^2 \right)^{1/2}, \quad (4.40)$$

$$A_2 N_2 = \pm \left(\frac{a}{b_2} \left(\frac{5}{9} \frac{b_1^2}{ab_2} - k^2 \right) \right)^{1/2}, \quad (4.41)$$

$$v_2 = -2ak. \quad (4.42)$$

Physical interpretation of the parameters:

- $A_2 M_2$: Determines the background amplitude of the soliton (far from the soliton center).
- $A_2 N_2$: Controls the soliton depth (intensity dip relative to the background).
- B_2 : Represents the inverse width of the soliton (higher B_2 means a narrower soliton).
- v_2 : The propagation velocity of the soliton.
- Ω : Effective frequency shift of the soliton due to nonlinearity and dispersion.

Conditions for existence:

$$\frac{5}{9} \frac{b_1^2}{ab_2} - k^2 \geq 0, \quad (4.43)$$

which ensures that B_2 and $A_2 N_2$ are real. This implies:

- a and b_2 must be nonzero and have the same sign (i.e., $a/b_2 > 0$).
- The term $\frac{5}{9} \frac{b_1^2}{ab_2}$ must be greater than or equal to k^2 , limiting the admissible values of the wave number k .

Thus, the dark soliton exists on a non-zero background and is characterized by a localized intensity dip propagating with velocity $v_2 = -2ak$. The existence of solitonic solutions is governed by the threshold $b_1 = -4$, at which the tanh-dependent term vanishes because $A_2 N_2 = 0$, reducing the solution to a trivial plane wave. For repulsive interactions, the condensate supports dark soliton, manifested as localized density depressions (“notches”) that propagate stably without dispersion. The depth of the soliton core increases with

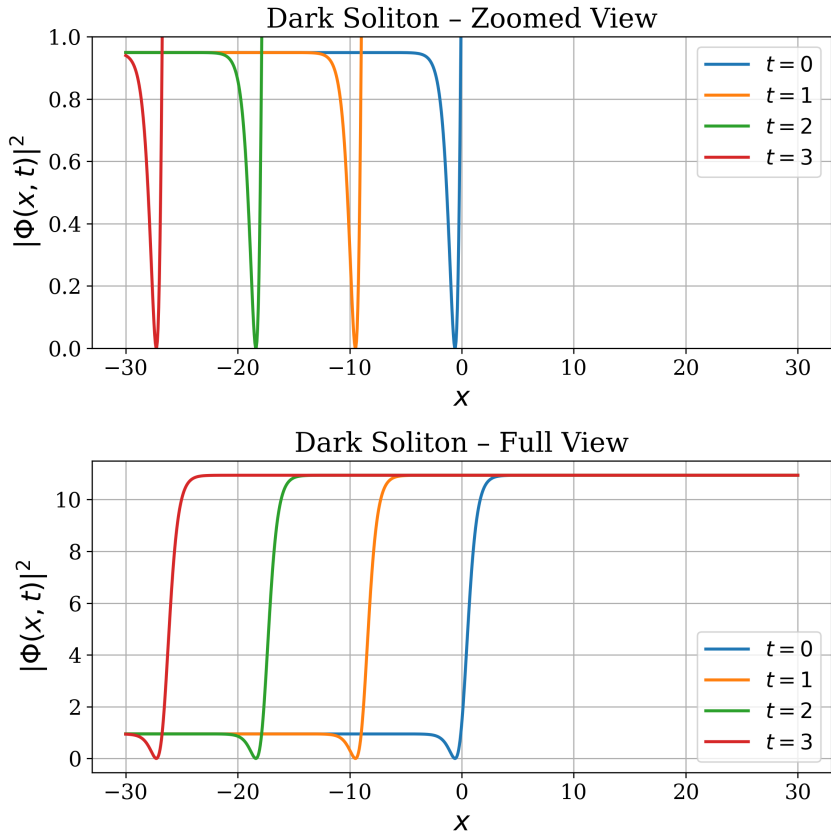


Figure 4.5: Propagation of the dark soliton in the negative x -direction. The soliton maintains a constant width and depth during its motion, indicating stable propagation governed by the balance between dispersion and nonlinearity.

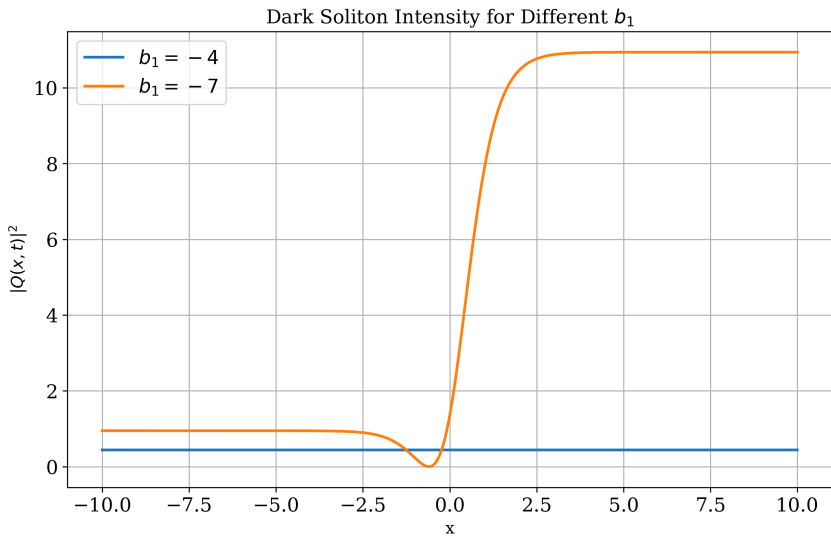


Figure 4.6: Threshold condition for the formation of a dark soliton. The parameter b_1 must be greater than or equal to -4 for a dark soliton to exist according to our ansatz. At $b_1 = -4$, the solution becomes trivial, resulting in plain plane waves, which are represented by the straight line.

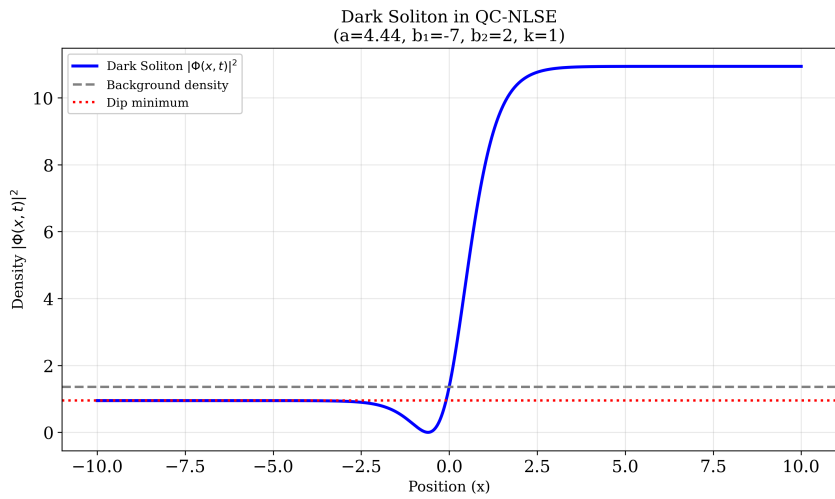


Figure 4.7: Plot showing the density of the dark soliton profile, background density and Dip minimum

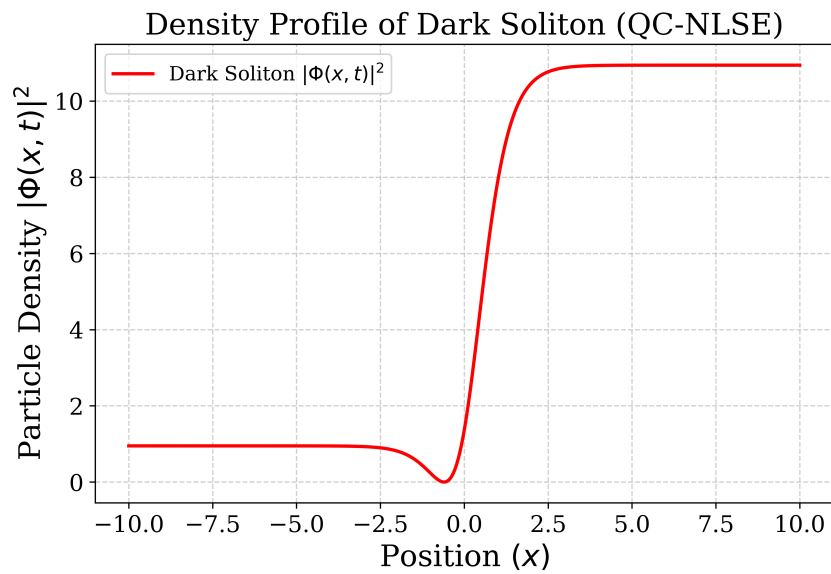


Figure 4.8: Density profile of the dark soliton.

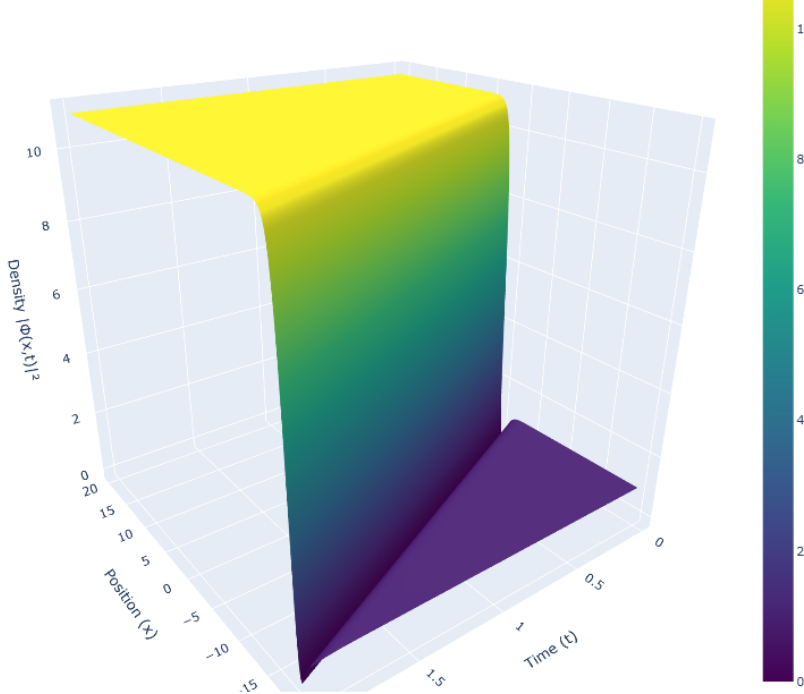


Figure 4.9: Three-dimensional representation of a propagating dark soliton.

$|b_1|$, reflecting the growth of A_2N_2 . The flat background density on either side of the dip corresponds to the uniform condensate, while the localized depression is accompanied by a characteristic phase slip of the wavefunction. The smoothness of the density profile highlights the underlying quantum coherence, and the robust propagation confirms the balance between dispersion and nonlinear interactions.

4.3 Numerical Study of the Bose Einstein Condensate in an Optical Ratchet Potential

4.4 Split Operator Method

The dynamics of a Bose–Einstein condensate (BEC) in an external potential are governed by the one-dimensional time-dependent Gross–Pitaevskii equation (GPE):

$$i\hbar \frac{\partial \psi(x,t)}{\partial t} = \left[-\frac{\hbar^2}{2m} \frac{\partial^2}{\partial x^2} + V(x,t) + g|\psi(x,t)|^2 \right] \psi(x,t), \quad (4.44)$$

where $\psi(x,t)$ is the condensate wavefunction, $V(x,t)$ is the external potential, and g characterizes the strength of the non-linear interaction. To numerically integrate Eq. (4.44), the split-operator method is employed. This method is based on the Trotter–Suzuki decomposition [89], which allows the time-evolution operator to be factorized into contributions from the kinetic and potential parts of the Hamiltonian. Writing the Hamiltonian as:

$$\hat{H} = \hat{T} + \hat{V}, \quad \hat{T} = -\frac{\hbar^2}{2m} \nabla^2, \quad \hat{V} = V(x,t) + g|\psi(x,t)|^2, \quad (4.45)$$

the time-evolution operator over a small interval Δt can be approximated to second order as:

$$e^{-i\hat{H}\Delta t/\hbar} \approx e^{-i\hat{V}\Delta t/(2\hbar)} e^{-i\hat{T}\Delta t/\hbar} e^{-i\hat{V}\Delta t/(2\hbar)}. \quad (4.46)$$

The advantage of this decomposition is that \hat{V} is diagonal in real space, while \hat{T} is diagonal in momentum space. The kinetic term is applied in Fourier space using the Fast Fourier Transform (FFT) and its inverse, making the algorithm computationally efficient. Each time step is performed as follows:

1. Apply a half-step evolution under the potential and nonlinear interaction in real space.
2. Transform to momentum space using FFT, apply the kinetic evolution for a full step, and transform back to real space using the inverse FFT.
3. Apply another half-step under the potential and nonlinear interaction in real space.

This procedure ensures second-order accuracy and conserves the norm of the wavefunction throughout the simulation.

4.5 Implementation Details

The simulation was implemented in Python using NumPy and SciPy libraries. The main steps are summarized below:

- **Spatial and Momentum Grids:** A one-dimensional domain of length $L_x = 10$ is discretized into $N_x = 1024$ points with spacing $\Delta x = L_x/N_x$. The corresponding momentum space grid is constructed using the relation $k = \frac{2\pi}{L_x}n$, where n is an integer index.
- **Initial Condition:** The condensate is initialized as a normalized Gaussian wave packet:

$$\psi(x, 0) \propto e^{-x^2}.$$

- **External Potential:** A time-dependent ratchet potential is applied:

$$V(x, t) = V_0 [\sin(k_L x) + \alpha \sin(2k_L x + \phi)] \sin(2\pi t), \quad (4.47)$$

where V_0 is the potential depth, $k_L = 2\pi$ is the lattice wave vector, α controls the asymmetry, and $\phi = \pi/2$ is a phase shift.

- **Time Evolution:** The wavefunction is propagated for $N_t = 2000$ steps with a time step $\Delta t = 0.001$ using the split-operator method described in Eq. (4.46).
- **Data Output:** At regular intervals, the density profile $\rho(x, t) = |\psi(x, t)|^2$ is stored for visualization.

The code concludes by plotting the density evolution at selected times, providing insight into the condensate dynamics under the ratchet potential.

4.6 Time-Dependent Penrose–Onsager Analysis

To quantify condensation and fragmentation during dynamical evolution, we employ the time-dependent Penrose–Onsager criterion [90]. This method characterizes Bose–Einstein condensation via the eigenvalues of the one-body density matrix:

$$\rho(x, x') = \langle \hat{\Psi}^\dagger(x) \hat{\Psi}(x') \rangle. \quad (4.48)$$

In our numerical approach, the density matrix is constructed from the time-averaged wave functions stored during evolution:

$$\rho(x_i, x_j) \approx \frac{1}{M} \sum_{n=1}^M \psi^*(x_i, t_n) \psi(x_j, t_n) \Delta x, \quad (4.49)$$

where M is the number of stored snapshots. Diagonalization yields eigenvalues λ_k sorted in descending order. The largest eigenvalue λ_0 corresponds to the condensate mode, and the condensate fraction is:

$$n_c = \frac{\lambda_0}{\sum_k \lambda_k}, \quad n_{nc} = 1 - n_c, \quad (4.50)$$

where n_{nc} denotes the non-condensate fraction.

4.6.1 Physical Observables

To monitor the system’s evolution under the ratchet potential given by Eq. (4.47), we compute the following observables:

- **Energy Contributions:** Kinetic, interaction, and potential energies, defined as:

$$E_{\text{kin}} = \int \frac{|\partial_x \psi|^2}{2} dx, \quad (4.51)$$

$$E_{\text{int}} = \int \frac{g}{2} |\psi|^4 dx, \quad (4.52)$$

$$E_{\text{pot}} = \int V(x, t) |\psi|^2 dx, \quad (4.53)$$

with the total energy $E = E_{\text{kin}} + E_{\text{int}} + E_{\text{pot}}$.

- **Current:**

$$J = \int \text{Im} [\psi^*(x, t) \partial_x \psi(x, t)] dx, \quad (4.54)$$

which indicates directed transport.

- **Condensate and Non-Condensate Fractions:** Evaluated from the Penrose–Onsager method as described above.

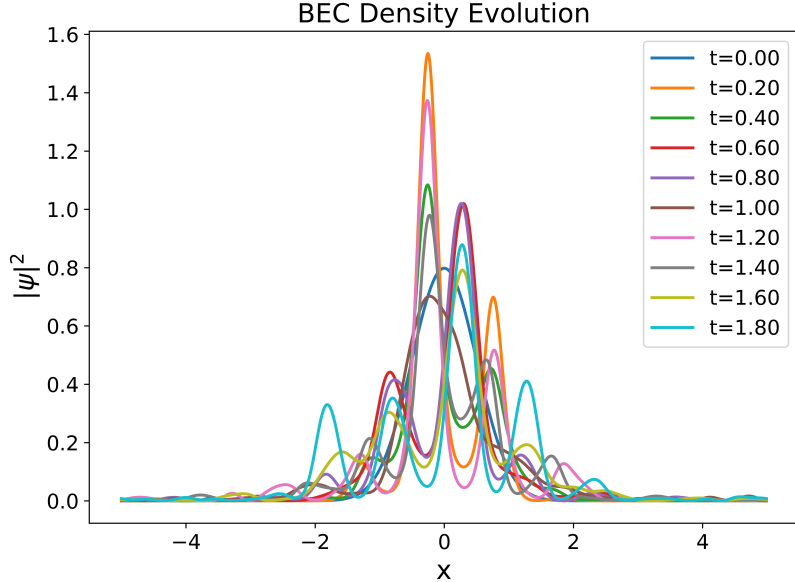


Figure 4.10: Density evolution on the wavefunction in 1D along the x axis at different time, under the influence of the ratchet potential

4.6.2 Numerical Results and Interpretations

4.6.3 Density Evolution

Figure 4.10 shows the evolution of the wavefunction density $|\psi(x)|^2$ along the x -axis in one dimension. At $t = 0$, the density profile is Gaussian and centered at $x = 0$. As time progresses, the time-modulated ratchet potential induces asymmetric kicks, causing the atoms to move preferentially in one direction. The nonlinearity $g|\psi|^2$ leads to self-interaction effects, resulting in wavepacket broadening and slight shape distortion, as evident in the figure. Notably, the wavepacket shifts directionally rather than spreading symmetrically. Figures 4.11 display three-dimensional simulations of the condensate density $|\psi(x, y, z = 0)|^2$, captured at the slice $z = 0$ for different times. At $t = 0$, the density peaks at the center and decays smoothly outward. Under the influence of the ratchet potential, the density develops periodic modulations (ripples) along x , y , and z , with peaks shifting preferentially in one direction. The nonlinear interactions cause additional effects; deformation and interference. The density no longer passively follows the lattice but forms local hotspots. Interference fringes arise from the competition between potential and kinetic energy where bright regions correspond to high atomic density and dark region reflects areas where atoms are repelled by potential barriers. In summary, the ratchet potential acts as a time varying 3D optical lattice with broken symmetry, driving directed transport. The $z = 0$ slice reveals how density modulation and redistribution emerge, even in a complex 3D wavefunction.

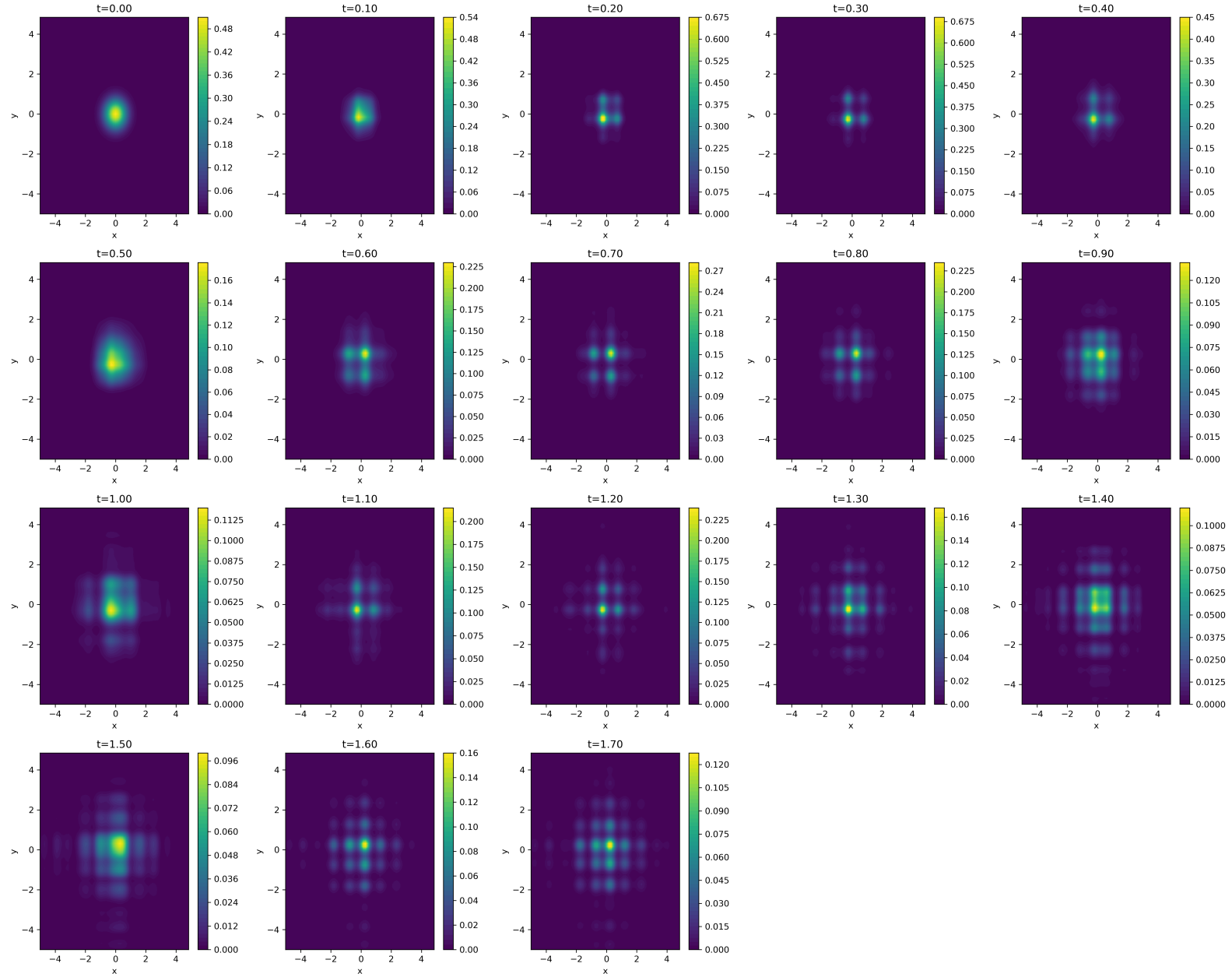


Figure 4.11: Slice of density evolution of a bright soliton in a 3D ratchet potential. The images show the evolution of the wavefunction density, sliced at $z=0$, over time from $t=0.00$ to $t=1.70$. The ratchet potential causes the soliton to move and spread, exhibiting complex dynamics and a periodic return to a similar state.

4.6.4 Condensate vs Non-Condensate Fraction

Figure 4.12, 4.13, 4.14 describes the dynamics between condensate and non condensate particles. From figure 4.13 we observe a rapid depletion of condensate fraction from nearly unity towards significantly lower values. The decay reflects the fragmentation of the initial coherent state into multiple occupied modes. The depletion process can be interpreted as a driven-dissipation less analogue of heating: the time-periodic potential acts as a coherent pump, and interactions redistribute this injected energy among available single-particle modes. The absence of any thermal bath means that once atoms leave the condensate mode, they remain in the excited fraction, leading to a monotonic decrease in condensate fraction. This behaviour is qualitatively similar to experimentally observed interaction-driven depletion in periodically driven BECs, where strong driving and significant nonlinearity lead to fragmentation of the macroscopic wavefunction [?, ?].

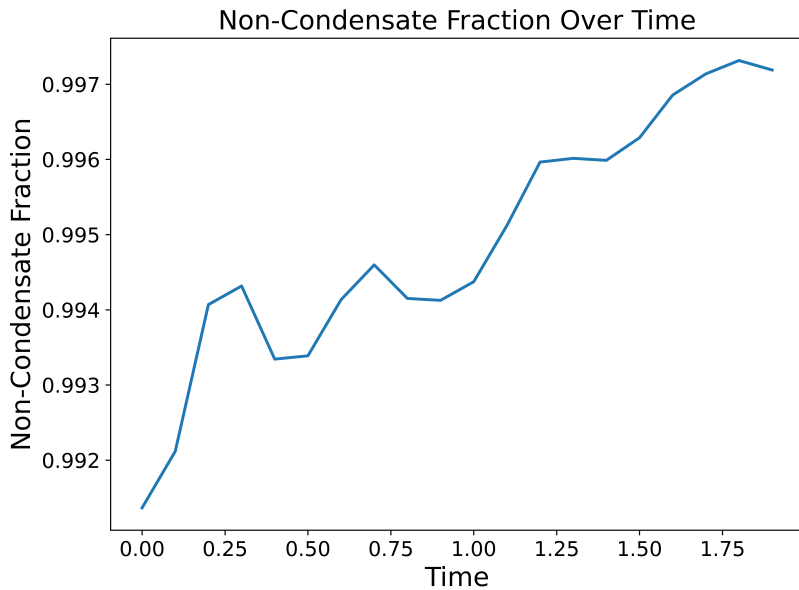


Figure 4.12: Time evolution of the non-condensate fraction. The fraction $f_{nc} = 1 - f_c$, where f_c is the condensate fraction obtained from the Penrose Onsager criterion, is shown as a function of simulation time. The increase reflects the progressive depletion of the condensate due to interaction-driven excitations induced by the time-dependent ratchet potential.

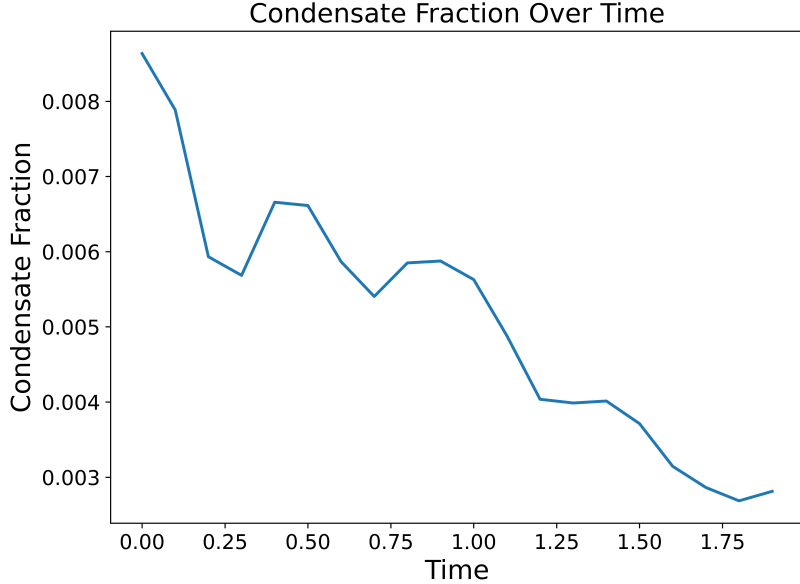


Figure 4.13: Time evolution of the condensate fraction. The fraction $f_{nc} = 1 - f_c$, where f_c is the condensate fraction obtained from the Penrose Onsager criterion, is shown as a function of simulation time. The sharp decrease reflects progressive depletion of the condensate due to interaction-driven excitations induced by the time-dependent ratchet potential.

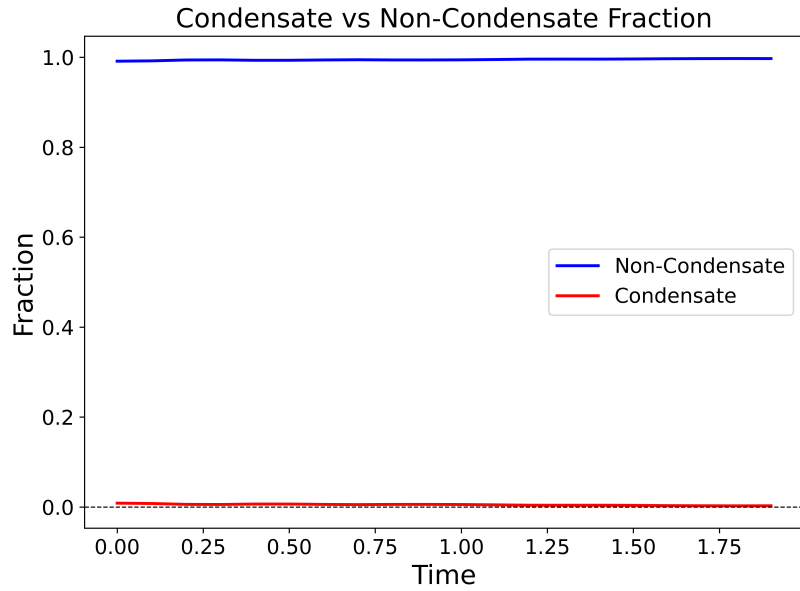


Figure 4.14: Time evolution of condensate and non-condensate fractions in a driven Bose-Einstein condensate. The plot demonstrates near-complete depletion of the condensate fraction (maintained near zero) with corresponding population growth in non-condensate modes (approaching unity), revealing strong fragmentation dynamics under periodic driving. This behavior characterizes the system's departure from coherence due to interaction-induced mode mixing.

4.6.5 Energy Contributions and their effect on condensate and non condensate fractions

Figure 4.15, 4.16, 4.17, 4.18, and 4.19 describe the energy contributions and their effect on the condensate and non condensate fraction. To get a clear insight on how the different energy components affect the condensate. Let us look at the data from the simulation for time $t = 0$ to time $t = 1.9$.

Table 4.1: Energy contributions at different times during the simulation.

Time t	Kinetic Energy	Interaction Energy	Potential Energy
0.000	0.500	0.282	0.000
0.100	1.233	0.287	-1.004
0.200	4.207	0.401	-5.369
0.300	3.713	0.394	-4.865
0.400	2.173	0.268	-1.761
0.500	1.507	0.212	0.003
0.600	2.401	0.260	-1.580
0.700	3.301	0.317	-3.782
0.800	2.824	0.255	-3.248
0.900	2.214	0.235	-1.507
1.000	1.521	0.215	-0.001
1.100	2.364	0.257	-1.910
1.200	3.733	0.313	-4.793
1.300	4.186	0.289	-5.185
1.400	2.599	0.225	-1.912
1.500	1.489	0.169	-0.004
1.600	1.841	0.178	-1.355
1.700	2.921	0.194	-3.412
1.800	3.940	0.199	-4.384
1.900	2.712	0.153	-1.727

The table above illustrates the temporal evolution of the kinetic, interaction, and potential energy components throughout the simulation. At the initial time $t=0$, the system exhibits moderate kinetic and interaction energies, while the potential energy is zero, reflecting the absence of the external ratchet potential. As the simulation progresses, a clear inverse relationship emerges between kinetic and potential energies: periods of high potential energy correspond to low kinetic energy, and vice versa. The potential energy reaches large negative values, indicative of the influence of the time-dependent ratchet potential, which imposes an asymmetric energy landscape that strongly modulates particle dynamics. The negative potential energy corresponds to instances where the wavefunction becomes highly localized within the minima of the potential, reflecting the transient trapping of particles.

These energy oscillations demonstrate that the system alternates between quasi-free states and localized states under the action of the ratchet forcing, as illustrated in Figure 4.22. During quasi-free states, the wavefunction extends over larger regions of space, behaving similarly to a free particle with minimal confinement. In contrast, the localized states display multiple peaks in the wavefunction, signifying that the atoms are effectively trapped

in the potential minima. This dynamic interplay between the particles and the time-dependent potential highlights how the ratchet potential can alternately suppress particle mobility and allow freer propagation, effectively controlling localization and transport.

Throughout the simulation, the interaction energy remains comparatively small and exhibits limited variation, suggesting that particle-particle interactions contribute less significantly to the overall energy dynamics than the kinetic and potential terms. The observed fluctuations in kinetic and potential energy are closely associated with changes in the condensate and non-condensate fractions. Periods of increased kinetic and potential energy correspond to enhanced excitation processes, resulting in depletion of the condensate and growth of the non-condensate component. Overall, these energy exchange mechanisms, predominantly driven by the external potential and kinetic excitations, play a central role in shaping the temporal evolution of the condensate and governing its dynamical behaviour.

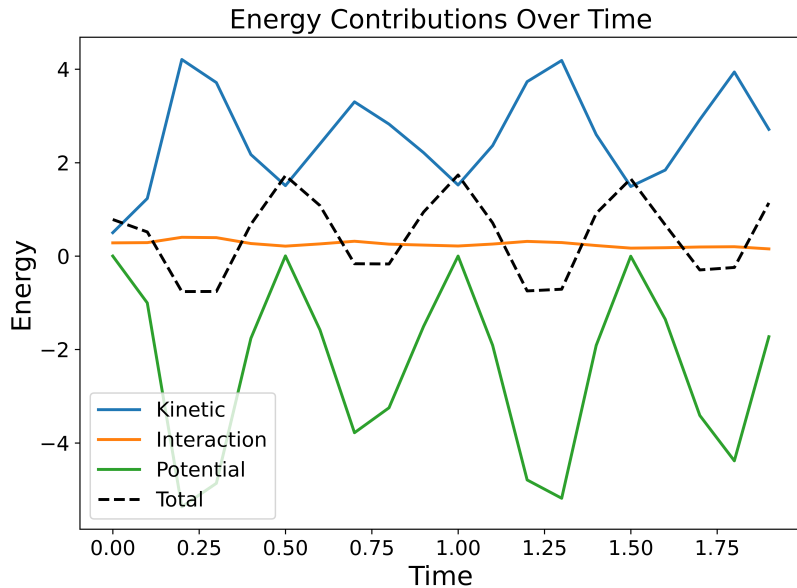


Figure 4.15: Time evolution of kinetic, interaction, and potential energies along with total energy. The external ratchet potential injects energy, leading to growth in kinetic and interaction energies which drive excitations and condensate depletion.

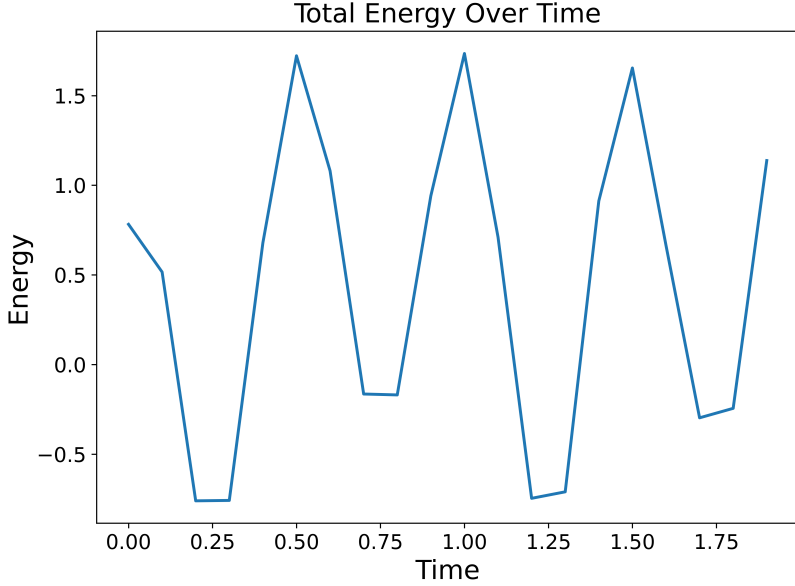


Figure 4.16: Temporal evolution of the system's total energy under a time-modulated ratchet potential. The monotonic increase in total energy demonstrates continuous energy injection from the external potential, which drives quantum excitations and mediates the transition from condensed to non-condensed states. The energy redistribution among kinetic (particle motion), potential (confinement effects), and interaction (inter-particle collisions) components reflects the dynamic balance between driving-induced excitations and the system's inherent nonlinearity. This energy transfer mechanism directly correlates with the observed condensate depletion dynamics shown in Figures 4.12-4.14.

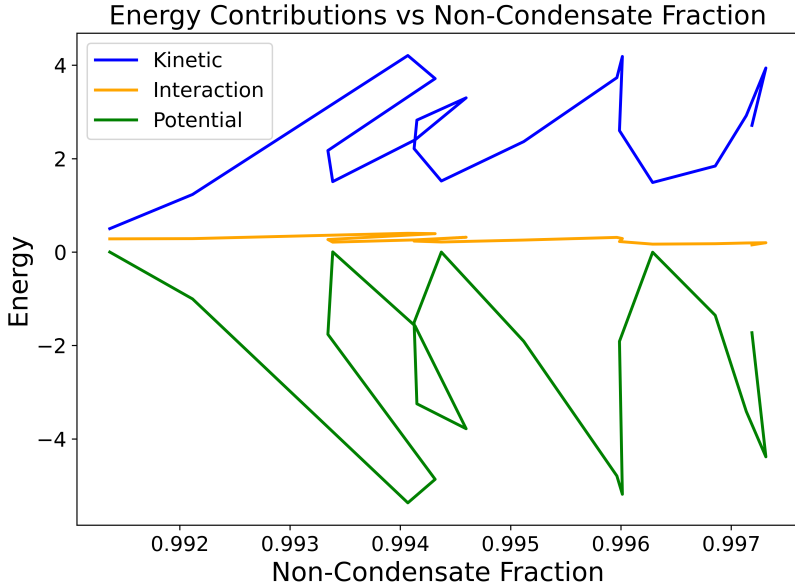


Figure 4.17: Kinetic, interaction, and potential energies plotted against the non-condensate fraction reveal how each energy term contributes to condensate depletion. Increasing kinetic and interaction energies correlate with higher non-condensate fractions, indicating enhanced excitation and scattering processes.

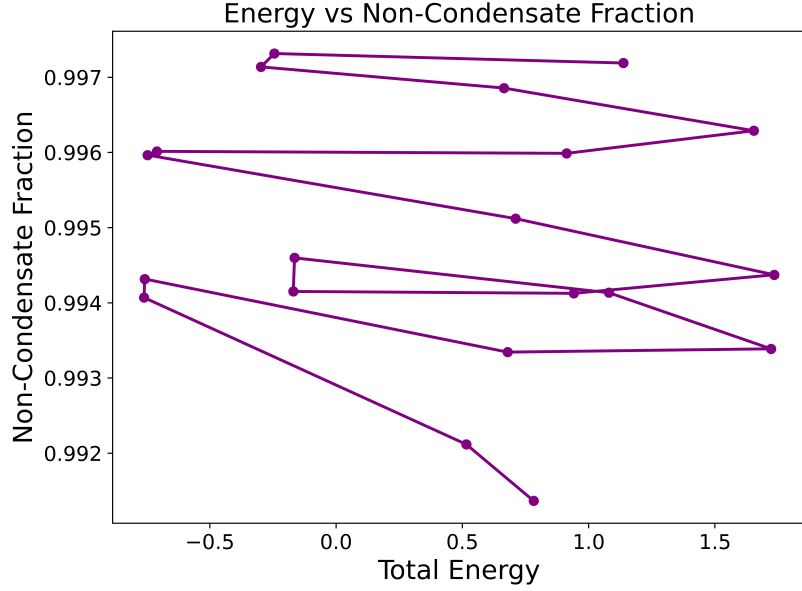


Figure 4.18: The diagram plots the non-condensate fraction against the total energy of a system. The data points, connected by lines, show a complex, non-monotonic relationship between these two quantities. The plot doesn't reveal a simple linear or easily predictable correlation, suggesting that the system's dynamics involve intricate energy exchanges and excitations that influence the partitioning between condensed and non-condensed states. The non-condensate fraction values are very high, ranging from approximately 0.992 to 0.997, indicating that the vast majority of particles in the system remain in a non-condensed (thermal) state throughout the observed energy range. This suggests that the Bose-Einstein condensate is being rapidly depleted. The total energy values span from roughly -0.75 to 1.75. The "zig-zag" pattern of the connected points implies that as the total energy fluctuates, the non-condensate fraction also undergoes variations, but not in a simple increasing or decreasing trend. This is indicative of the dynamic process where energy is constantly being exchanged between different modes within the system, leading to the observed non-linear behaviour.

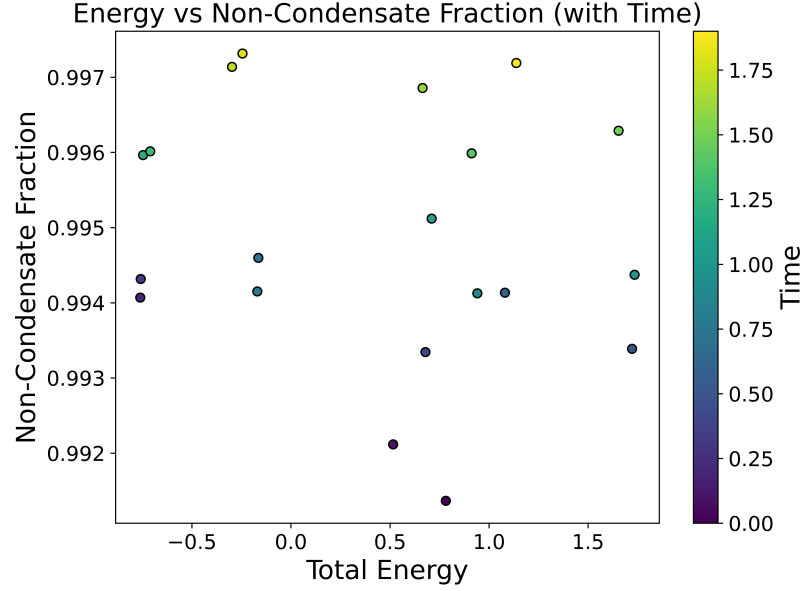


Figure 4.19: Time-resolved correlation between total energy and non-condensate fraction in a driven Bose-Einstein condensate. The color map reveals three dynamical regimes: (I) At low energies ($E \approx -1.75$ to -0.5), the system maintains high condensation (non-condensate fraction < 0.992); (II) Near $E \approx 0$, rapid fragmentation occurs as energy injection populates excited modes (non-condensate fraction 0.992–0.996); (III) For $E > 0.5$, saturation occurs with near-total depletion (0.996–0.997). The hysteresis-like path demonstrates memory effects in the energy-fragmentation relationship, where the condensate response lags behind energy changes due to interaction delays.

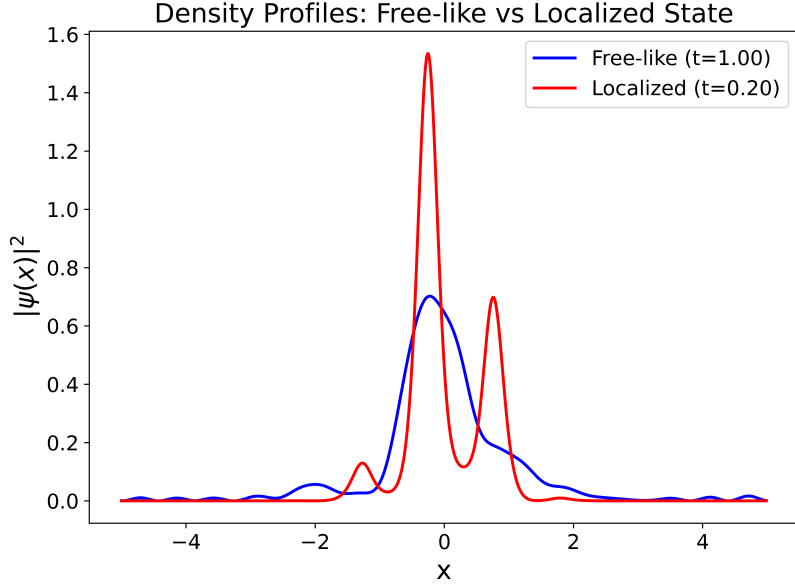


Figure 4.20: The spatial density profiles $|\psi(x)|^2$ demonstrating dynamical localization transitions induced by a time-periodic ratchet potential. Delocalized regime showing broad, gaussian-like density distribution, characteristic of quasi-free propagation when potential effects are minimal. Localized regime exhibiting sharp density peaks at the potential minimal. The atoms is confined within three potential wells. The transition between states is mediated by the ratchet potential amplitude and phase modulation, with localization occurring when the potential depth exceeds the kinetic energy.

4.6.6 Current and average motion of the condensate

Figures 4.21 and 4.22 present the time evolution of the quantum mechanical current $J(t)$, computed as the spatial integral of the probability current density obtained from the wavefunction $\psi(x, t)$. The quantity $J(t)$ characterises the net particle flow induced by the time-dependent ratchet potential. At early times, fluctuations in $J(t)$ reflect the immediate dynamical response of the condensate to the driving potential and interparticle interactions. As the evolution progresses, a sustained non-zero average current develops, indicating directed particle transport in the absence of an overall bias force. The $J(t)$ alternates between positive and negative values with a period matching the ratchet potential driving frequency ($\omega = 2\pi$). This directed motion originates from the asymmetry of the ratchet potential combined with non-linear interaction effects, and it exemplifies the dynamic transition between localized (trapped) and free-like (delocalized) states within the condensate. The cumulative average current provides an additional measure of the net transport efficiency throughout the simulation.

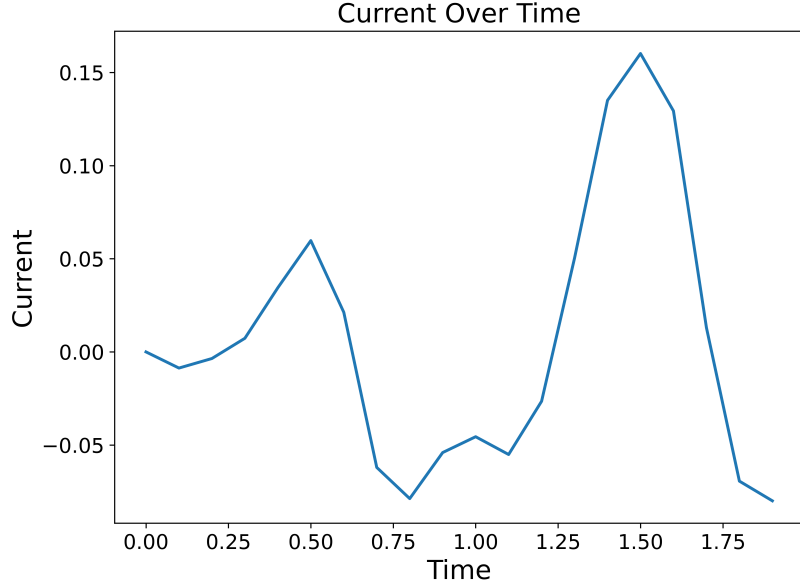


Figure 4.21: Time evolution of the instantaneous quantum mechanical current $J(t)$, calculated as the spatial integral of the probability current density derived from the wavefunction $\psi(x, t)$. The fluctuations observed at early times reflect the condensate's initial dynamical response to the time-dependent ratchet potential and inter-particle interactions. As the simulation progresses, a sustained non-zero current develops, indicating directed particle transport in the absence of an overall bias force.

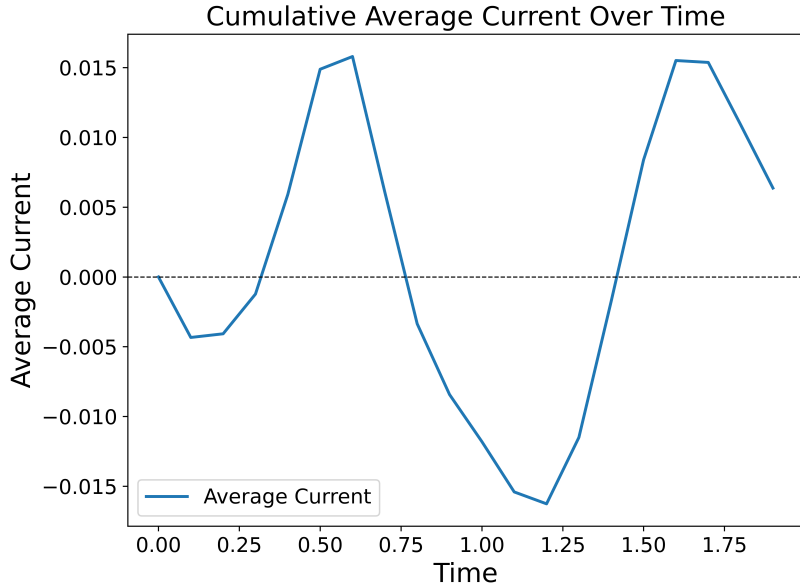


Figure 4.22: Time evolution of the cumulative average quantum mechanical current, defined as $\bar{J}(t) = \frac{1}{t} \int_0^t J(t') dt'$, which quantifies the net transport efficiency over time. The emergence of a non-zero asymptotic value reflects the persistent directed motion induced by the asymmetric ratchet potential in combination with non-linear interaction effects, illustrating the transition between localized and free-like states in the condensate.

4.7 Conclusion

The Gross–Pitaevskii equation (GPE) provides a powerful theoretical framework for studying the dynamics of ultracold atomic systems. In this work, we investigated two regimes of the GPE to explore the behavior of Bose–Einstein condensates (BECs). The first regime corresponds to the case $V=0$, where no external potential is present. In this limit, the condensate behaves like a freely propagating quantum wave packet. However, the motion is not entirely free: the balance between dispersion and nonlinear self-interaction stabilizes the shape of the wave packet over time. Under certain approximations, our analysis shows that the condensate can propagate without distortion over long timescales. Analytically, we obtained both bright and dark soliton solutions to the GPE in this regime. These soliton solutions illustrate that, even in the absence of an external potential, nonlinear interactions can support robust, localized wave structures that preserve their form during propagation—demonstrating the wave-like nature of the condensate arising from the interplay between dispersion and interaction effects.

In the second regime, we performed a numerical investigation of a three-dimensional BEC evolving under the influence of an asymmetric, time-dependent ratchet potential. This configuration reveals a rich interplay between interaction-driven excitations, symmetry breaking, and transport phenomena. The condensate fraction, evaluated via the Penrose–Onsager criterion, exhibits a gradual decrease over time, while the complementary non-condensate fraction increases correspondingly. This behaviour indicates the progressive depletion of the macroscopic coherent state as energy is transferred into excited modes, driven by the combined effects of temporal modulation in the potential and interparticle interactions.

An analysis of the system’s energetics shows that kinetic, interaction, and potential energy components undergo pronounced oscillations in phase with the periodic driving. Peaks in kinetic energy correlate with reductions in potential energy, signifying particle release from localized regions into extended, free-like states. Conversely, minima in kinetic energy coincide with enhanced potential energy, reflecting stronger particle confinement within the trap.

The time evolution of the quantum mechanical current, computed as the spatial integral of the probability current density derived from the condensate wavefunction, confirms the emergence of directed transport. Initially dominated by transient fluctuations, the current develops a sustained, non-zero average, revealing net particle flow even in the absence of a static bias force. This directed motion is a direct consequence of the broken spatial inversion symmetry of the ratchet potential combined with temporal driving, which together break detailed balance and induce preferential motion. The cumulative average current provides a quantitative measure of transport efficiency in this nonequilibrium setting.

Overall, the results presented in this chapter demonstrate that time-dependent ratchet potentials can be used to induce and control transport in condensates while dynamically modulating the balance between localized and delocalized states. This work provides both qualitative insight and quantitative benchmarks for understanding nonequilibrium phenomena in interacting quantum fluids, and offers a foundation for future studies involving

more complex driving protocols, stronger interaction regimes, and multi-component condensate systems.

4.8 Future Outlook

The study of Bose–Einstein condensates (BECs) subjected to time-dependent ratchet potentials has revealed intricate dynamical behaviors and rich transport phenomena, highlighting the need for further investigation [91]. Extending these analyses to regimes with stronger interparticle interactions or higher-dimensional ratchet geometries could more closely approximate realistic experimental conditions and elucidate new aspects of condensate dynamics. The inclusion of multi-component or spinor condensates may uncover novel couplings between internal degrees of freedom and ratchet-induced transport, potentially enabling controlled spin currents or the emergence of exotic quantum phases.

Moreover, implementing more complex temporal modulations and spatial asymmetries in the ratchet potential could improve the tunability and efficiency of directed transport, advancing the design of quantum ratchet devices with tailored functionalities. Investigating the behavior of these driven condensates in dissipative environments or within optical lattices containing disorder would shed light on the robustness of transport mechanisms against decoherence and external noise—an essential consideration for practical quantum technologies.

Finally, ongoing advances in experimental techniques that enable high-resolution probing of nonequilibrium condensate dynamics will be crucial for validating theoretical predictions and simulations. Such studies promise to deepen our understanding of quantum transport in driven many-body systems. The integration of theoretical modeling, numerical simulations, and precise experiments will facilitate the use of BECs as quantum simulators and inform future applications in atomtronics and quantum information processing.

References

- [1] F. F. Chen, *Introduction to Plasma Physics and Controlled Fusion*, 3rd ed., Springer, 2016.
- [2] Bose. "Plancks gesetz und lichtquantenhypothese." *Zeitschrift für Physik* 26.1 (1924): 178-181.
- [3] Einstein, Albert. Quantentheorie des einatomigen idealen Gases: Abhandlung 2. 1925.
- [4] Anderson, Mike H., et al. "Observation of Bose-Einstein condensation in a dilute atomic vapor." *science* 269.5221 (1995): 198-201.
- [5] Griffiths, David. *Introduction to elementary particles*. John Wiley and Sons, 2020.
- [6] A Zyla, P., et al. "Review of Particle Physics (RPP 2020)." *PROGRESS OF THEORETICAL AND EXPERIMENTAL PHYSICS* 2020.8 (2020): 1-2093.
- [7] Close, Frank E. *The Infinity Puzzle: Quantum Field Theory and the Hunt for an Orderly Universe*. Basic Books (AZ), 2011.
- [8] Pauli, Wolfgang. "Über den Zusammenhang des Abschlusses der Elektronengruppen im Atom mit der Komplexstruktur der Spektren." *Zeitschrift für Physik* 31.1 (1925): 765-783.
- [9] Higgs, Peter W. "Broken symmetries and the masses of gauge bosons." *Physical review letters* 13.16 (1964): 508.
- [10] Dalfovo, Franco, et al. "Theory of Bose-Einstein condensation in trapped gases." *Reviews of modern physics* 71.3 (1999): 463.
- [11] Anderson, Mike H., et al. "Observation of Bose-Einstein condensation in a dilute atomic vapor." *science* 269.5221 (1995): 198-201.
- [12] Davis, Kendall B., et al. "Bose-Einstein condensation in a gas of sodium atoms." *Physical review letters* 75.22 (1995): 3969.
- [13] Pethick, Christopher J., and Henrik Smith. *Bose-Einstein condensation in dilute gases*. Cambridge university press, 2008.
- [14] Dalfovo, Franco, et al. "Theory of Bose-Einstein condensation in trapped gases." *Reviews of modern physics* 71.3 (1999): 463.
- [15] Gross, Eugene P. "Structure of a quantized vortex in boson systems." *Il Nuovo Cimento (1955-1965)* 20.3 (1961): 454-477.

- [16] Pitaevskii, Lev P. "Vortex lines in an imperfect Bose gas." Sov. Phys. JETP 13.2 (1961): 451-454.
- [17] Bradley, Curtis Charles, C. A. Sackett, and R. G. Hulet. "Bose-Einstein condensation of lithium: Observation of limited condensate number." Physical Review Letters 78.6 (1997): 985.
- [18] Stoof, Henk TC. "Coherent versus incoherent dynamics during Bose-Einstein condensation in atomic gases." Journal of low temperature physics 114.1 (1999): 11-108.
- [19] Shi, Hualin, and Wei-Mou Zheng. "Bose-Einstein condensation in an atomic gas with attractive interactions." Physical Review A 55.4 (1997): 2930.
- [20] Salasnich, Luca. "Self-trapping, quantum tunneling, and decay rates for a Bose gas with attractive nonlocal interaction." Physical Review A 61.1 (1999): 015601.
- [21] Pérez-García, V. M., et al. (1997). "Analysis of an atom soliton laser based on the spatial modulation of the trapping potential." Physica D: Nonlinear Phenomena, 103(1-4), 82-94.
- [22] Pitaevskii, L., and S. Stringari, *Bose-Einstein Condensation and Superfluidity*, Oxford University Press, 2016.
- [23] Fetter, A. L., "Rotating trapped Bose-Einstein condensates," *Reviews of Modern Physics*, vol. 81, no. 2, pp. 647–691, 2009.
- [24] Fetter, Alexander L., and John Dirk Walecka. Quantum theory of many-particle systems. Courier Corporation, 2012.
- [25] Olshanii, Maxim. "Atomic scattering in the presence of an external confinement and a gas of impenetrable bosons." Physical review letters 81.5 (1998): 938.
- [26] Petrov, D. S., G. V. Shlyapnikov, and J. T. M. Walraven. "Regimes of quantum degeneracy in trapped 1D gases." Physical Review Letters 85.18 (2000): 3745.
- [27] Dunjko, Vanja, Vincent Lorent, and Maxim Olshanii. "Bosons in cigar-shaped traps: Thomas-Fermi regime, Tonks-Girardeau regime, and in between." Physical Review Letters 86.24 (2001): 5413.
- [28] Greiner, Markus, et al. "Quantum phase transition from a superfluid to a Mott insulator in a gas of ultracold atoms." nature 415.6867 (2002): 39-44.
- [29] Matthews, Michael Robin, et al. "Vortices in a Bose-Einstein condensate." Physical Review Letters 83.13 (1999): 2498.
- [30] Landau, Lev D., and Evgenij M. Lifshitz. "Fluid mechanics 2nd ed." Course of Theoretical Physics 6 (1987).
- [31] Shi, Chunxiao, et al. "Topological defects of spin-orbit coupled bose-einstein condensates in a rotating anharmonic trap." Journal of the Physical Society of Japan 87.9 (2018): 094003.
- [32] Allen, Les, et al. "Orbital angular momentum of light and the transformation of Laguerre-Gaussian laser modes." Physical review A 45.11 (1992): 8185.

- [33] Soskin, M. S., and M. V. Vasnetsov. "Singular optics." *Progress in optics*. Vol. 42. Elsevier, 2001. 219-276.
- [34] Yao, Alison M., and Miles J. Padgett. "Orbital angular momentum: origins, behavior and applications." *Advances in optics and photonics* 3.2 (2011): 161-204.
- [35] Pelton, Matthew, Javier Aizpurua, and Garnett Bryant. "Metal-nanoparticle plasmonics." *Laser and Photonics Reviews* 2.3 (2008): 136-159.
- [36] Molina-Terriza, Gabriel, Juan P. Torres, and Lluis Torner. "Twisted photons." *Nature physics* 3.5 (2007): 305-310.
- [37] Grier, David G. "A revolution in optical manipulation." *nature* 424.6950 (2003): 810-816.
- [38] Andersen, M. F., et al. "Quantized rotation of atoms from photons with orbital angular momentum." *Physical review letters* 97.17 (2006): 170406.
- [39] Fetter, Alexander L. "Rotating trapped bose-einstein condensates." *Reviews of Modern Physics* 81.2 (2009): 647-691.
- [40] Abo-Shaeer, Jamil R., et al. "Observation of vortex lattices in Bose-Einstein condensates." *Science* 292.5516 (2001): 476-479.
- [41] Madison, Kirk W., et al. "Vortex formation in a stirred Bose-Einstein condensate." *Physical review letters* 84.5 (2000): 806.
- [42] Coddington, I., et al. "Driving Bose-Einstein-Condensate Vorticity with a Rotating Normal Cloud." *Physical Review Letters* 87.21 (2003).
- [43] Scherer, David R., et al. "Vortex formation by merging of multiple trapped Bose-Einstein condensates." *Physical review letters* 98.11 (2007): 110402.
- [44] Anderson, B. P., et al. "Watching dark solitons decay into vortex rings in a Bose-Einstein condensate." *Physical Review Letters* 86.14 (2001): 2926.
- [45] Kivshar, Yuri S., and Govind P. Agrawal. *Optical solitons: from fibers to photonic crystals*. Academic press, 2003.
- [46] Agrawal, Govind P. "Nonlinear fiber optics." *Nonlinear Science at the Dawn of the 21st Century*. Berlin, Heidelberg: Springer Berlin Heidelberg, 2000. 195-211.
- [47] Khaykovich, L., et al. "Formation of a matter-wave bright soliton." *Science* 296.5571 (2002): 1290-1293.
- [48] Strecker, Kevin E., et al. "Formation and propagation of matter-wave soliton trains." *Nature* 417.6885 (2002): 150-153.
- [49] Ablowitz, Mark J. *Nonlinear dispersive waves: asymptotic analysis and solitons*. Vol. 47. Cambridge University Press, 2011.
- [50] Korteweg, Diederik Johannes, and Gustav De Vries. "XLI. On the change of form of long waves advancing in a rectangular canal, and on a new type of long stationary waves." *The London, Edinburgh, and Dublin Philosophical Magazine and Journal of Science* 39.240 (1895): 422-443.

- [51] Hasegawa, Akira, and Frederick Tappert. "Transmission of stationary nonlinear optical pulses in dispersive dielectric fibers. I. Anomalous dispersion." *Applied Physics Letters* 23.3 (1973): 142-144.
- [52] Washimi, Haruichi, and Tosiya Taniuti. "Propagation of ion-acoustic solitary waves of small amplitude." *Physical Review Letters* 17.19 (1966): 996.
- [53] Davydov, Alexander S. "The theory of contraction of proteins under their excitation." *Journal of Theoretical Biology* 38.3 (1973): 559-569.
- [54] Remoissenet, Michel. *Waves called solitons: concepts and experiments*. Springer Science and Business Media, 2013.
- [55] Erementchouk, M. V., L. I. Deych, and A. A. Lisyansky. "Spectral properties of exciton polaritons in one-dimensional resonant photonic crystals." *Physical Review B—Condensed Matter and Materials Physics* 73.11 (2006): 115321.
- [56] Mollenauer, Linn F., Roger H. Stolen, and James P. Gordon. "Experimental observation of picosecond pulse narrowing and solitons in optical fibers." *Physical review letters* 45.13 (1980): 1095.
- [57] Eiermann, B., et al. "Bright Bose-Einstein gap solitons of atoms with repulsive interaction." *Physical review letters* 92.23 (2004): 230401.
- [58] Frantzeskakis, D. J. "Dark solitons in atomic Bose-Einstein condensates: from theory to experiments." *Journal of Physics A: Mathematical and Theoretical* 43.21 (2010): 213001.
- [59] Burger, Stefan, et al. "Dark solitons in Bose-Einstein condensates." *Physical Review Letters* 83.25 (1999): 5198.
- [60] Denschlag, J., et al. "Generating solitons by phase engineering of a Bose-Einstein condensate." *Science* 287.5450 (2000): 97-101.
- [61] Anderson, B. P., et al. "Watching dark solitons decay into vortex rings in a Bose-Einstein condensate." *Physical Review Letters* 86.14 (2001): 2926.
- [62] Becker, Christoph, et al. "Oscillations and interactions of dark and dark–bright solitons in Bose–Einstein condensates." *Nature Physics* 4.6 (2008): 496-501.
- [63] Kazansky, A. K. "A computational scheme for the non-stationary treatment of two-electron processes." *Journal of Physics B: Atomic, Molecular and Optical Physics* 31.14 (1998): L579.
- [64] Hemmers, Oliver, et al. "Beyond the dipole approximation: angular-distribution effects in valence photoemission." *Journal of Physics B: Atomic, Molecular and Optical Physics* 30.21 (1997): L727.
- [65] Hakim, Vincent. "Nonlinear Schrödinger flow past an obstacle in one dimension." *Physical Review E* 55.3 (1997): 2835.
- [66] Engels, P., and C. Atherton. "Stationary and Nonstationary Fluid Flow of a Bose-Einstein Condensate? format?; Through a Penetrable Barrier." *Physical review letters* 99.16 (2007): 160405.

- [67] Weller, A., et al. "Experimental observation of oscillating and interacting matter wave dark solitons." *Physical review letters* 101.13 (2008): 130401.
- [68] Fedichev, P. O., A. E. Muryshev, and Gora V. Shlyapnikov. "Dissipative dynamics of a kink state in a Bose-condensed gas." *Physical Review A* 60.4 (1999): 3220.
- [69] Kuznetsov, E. A., and S. K. Turitsyn. "Instability and collapse of solitons in media with a defocusing nonlinearity." *Zh. Eksp. Teor. Fiz.* 94 (1988): 129.
- [70] Mamaev, A. V., M. Saffman, and A. A. Zozulya. "Propagation of dark stripe beams in nonlinear media: snake instability and creation of optical vortices." *Physical review letters* 76.13 (1996): 2262.
- [71] Crisp, Michael D. "Relativistic neoclassical radiation theory." *Physical Review A* 54.1 (1996): 87.
- [72] Maleshkov, G., et al. "Fractional vortex dipoles of edge-screw type in self-focusing Kerr nonlinear media." *16th International School on Quantum Electronics: Laser Physics and Applications*. Vol. 7747. SPIE, 2011.
- [73] Feder, David L., et al. "Anomalous modes drive vortex dynamics in confined Bose-Einstein condensates." *Physical Review Letters* 86.4 (2001): 564.
- [74] Jackson, B., J. F. McCann, and C. S. Adams. "Vortex line and ring dynamics in trapped Bose-Einstein condensates." *Physical Review A* 61.1 (1999): 013604.
- [75] Pitaevskii, L. P., and S. Stringari. "Bose-Einstein Condensation, Clarendon." (2003).
- [76] Dutton, Zachary, et al. "Observation of quantum shock waves created with ultra-compressed slow light pulses in a Bose-Einstein condensate." *Science* 293.5530 (2001): 663-668.
- [77] Henning, Patrick, and Elias Jarlebring. "The Gross-Pitaevskii equation and eigenvector nonlinearities: numerical methods and algorithms." *SIAM Review* 67.2 (2025): 256-317.
- [78] W. Bao and Q. Du, "Computational models for Bose-Einstein condensates," *Computational Physics Communications*, vol. 159, no. 1, pp. 1–19, 2004.
- [79] Javanainen, Juha, and Janne Ruostekoski. "Symbolic calculation in development of algorithms: split-step methods for the Gross-Pitaevskii equation." *Journal of Physics A: Mathematical and General* 39.12 (2006): L179.
- [80] Von Smoluchowski, Marian. "Experimental nachweisbare, der üblichen thermodynamik widersprechende molekularphänomene." *Phys. Zeitchrift* 13 (1912): 1069.
- [81] Feynman, Richard Phillips, Robert B. Leighton, and Matthew Linzee Sands. *The Feynman's Lectures on Physics*. Addison-Wesley, 1963.
- [82] Howard, Jonathon. "Mechanics of motor proteins." *Physics of bio-molecules and cells. Physique des biomolécules et des cellules: session LXXV. 2–27 July 2001. Berlin, Heidelberg*: Springer Berlin Heidelberg, 2002. 69-94.

- [83] Reimann, Peter. "Brownian motors: noisy transport far from equilibrium." Physics reports 361.2-4 (2002): 57-265.
- [84] Mateos, José L. "Chaotic transport and current reversal in deterministic ratchets." Physical Review Letters 84.2 (2000): 258.
- [85] Salger, Tobias, et al. "Directed transport of atoms in a Hamiltonian quantum ratchet." Science 326.5957 (2009): 1241-1243.
- [86] Dana, Itzhack, et al. "Experimental realization of quantum-resonance ratchets at arbitrary quasimomenta." Physical review letters 100.2 (2008): 024103.
- [87] Mendonça, J. T. "Self-phase modulation and superfluidity in twisted fluids of light." Europhysics Letters 129.6 (2020): 64004.
- [88] Stamper-Kurn, D. M., Miesner, H.-J., Chikkatur, A. P., Inouye, S., Stenger, J., and Ketterle, W. (1998). Reversible formation of a Bose-Einstein condensate. Physical Review Letters, 81(11), 2194–2197. <https://doi.org/10.1103/PhysRevLett.81.2194>
- [89] Suzuki, Masuo. "Decomposition formulas of exponential operators and Lie exponents with some applications to quantum mechanics and statistical physics." Journal of mathematical physics 26.4 (1985): 601-612.
- [90] Penrose, Oliver, and Lars Onsager. "Bose-Einstein condensation and liquid helium." Physical Review 104.3 (1956): 576.
- [91] Pérez-García, V. M., Michinel, H., Cirac, J. I., Lewenstein, M., and Zoller, P. (1997). Dynamics of Bose-Einstein condensates: Variational solutions of the Gross-Pitaevskii equations. Physical Review A, 56(2), 1424–1432. <https://doi.org/10.1103/PhysRevA.56.1424>